JOURNAL OF SOLID STATE CHEMISTRY **141,** 29–49 (1998)
ARTICLE NO. SC987903

Cristobalite-Related Oxide Structures

John G. Thompson,[1] Ray L. Withers, Stephen R. Palethorpe, and Alexandra Melnitchenko

Research School of Chemistry, Australian National University, Canberra, ACT 0200, Australia

Received October 27, 1997; in revised form May 22, 1998; accepted May 26, 1998

Cristobalite-related oxide structures are reviewed and described in terms of concerted rotations of $\langle 110\rangle_p$ (p = *C*9 parent structure) tetrahedral strings about two mutually orthogonal $\langle 110\rangle_p$ axes. All known structures are classified according to their patterns of rotations. This simple mechanism of distortion from *C*9 is the same as that proposed for the dynamically disordered model of *β*-cristobalite. Only fully Na stuffed *α*-cristobalite-type and *β*-$NaFeO_2$-type structures behave as if they comprise regular, rigid tetrahedra. The collapse of the various structures from their *C*9 parent and the regularity of the resultant tetrahedra are investigated. In fully or partly stuffed structures it is the size of the interstitial cations which determines the degree of collapse of the *C*9 framework.

1. INTRODUCTION

Many technologically important crystalline materials have framework structures. Examples are zeolites and perovskite-related ferroelectrics. There are also a number of geologically important framework structures, such as feldspars. What these examples have in common is that they each represent not just one structure but families of closely related structures.

Framework structures are almost invariably characterized by twofold coordination of apical atoms which are strongly bonded only to the atoms at the centers of the two polyhedra they connect. Other bonding interactions, such as those with interstitial atoms or adjacent polyhedra, are significantly weaker. While the individual polyhedra are relatively rigid the frameworks are quite flexible. The families of structures arise from the ability of these frameworks to distort in different ways while maintaining the connectivity of the polyhedra. Nearly all known framework structures comprise either octahedra, e.g., perovskite-type, or tetrahedra, e.g., zeolites, feldspars, and the silica polymorphs.

Cristobalite-related oxides, the subject of this review, are but one example of a family of framework structures with a common underlying parent structure. In this case the parent structure is a simple tetrahedral framework with cubic symmetry known as the *C*9 structure type (Fig. 1), originally proposed by Wyckoff as the structure of *β*-cristobalite (1, 2).

Cristobalite-related structures were first reviewed comprehensively by O'Keeffe and Hyde (3). The subject of this review included sulfides, phosphides, nitrides, halides, as well as oxides. A key aspect of this work was their proposed model for the structure of *β*-cristobalite based on multiple twinning of an $I\bar{4}2d$ symmetry model derived from the *C*9 structure by a concerted pattern of rotations of SiO_4 tetrahedra about their $\bar{4}$ axes. They also derived *α*-cristobalite-type structures with $P4_12_12$ symmetry and *β*-$NaFeO_2$-type structures with $Pna2_1$ symmetry by different patterns of rotations of SiO_4 tetrahedra about their $\bar{4}$ axes.

Since this review there have been two important developments. First, there have been many experimental and theoretical studies of *β*-cristobalite leading to a much better understanding of its somewhat enigmatic structure. Second, several cristobalite-related structure types have been discovered which were not known at the time of the previous review.

For the benefit of readers unfamiliar with the controversy surrounding the structure of *β*-cristobalite, a brief summary is now provided.

β- or high-cristobalite is the stable polymorph of SiO_2 between the melt at $\sim$2000 K down to 1743 K. It exists in a metastable form down to about 543 K when it undergoes a rapid and reversible transition to *α*- or low-cristobalite. *β*-Cristobalite has cubic symmetry with space group $Fd\bar{3}m$ and a cubic unit cell dimension of 7.17 Å just above the phase transition. For the structure to be ordered in this space group, however, the Si atoms must be located on the 8(*a*) sites and the O atoms on the 16(*c*) sites, corresponding to the *C*9 structure of Wyckoff.

The problem with the 7.17 Å *C*9 structure is that it has implausibly short Si–O bond lengths of $\sim$1.55 Å and Si–O–Si angles of 180°. To overcome this problem various authors have proposed microdomain models based on multiply twinned tetragonal microdomains to provide more chemically plausible local structures. Both Wright and

[1] To whom correspondence should be addressed.

0022-4596/98 $25.00

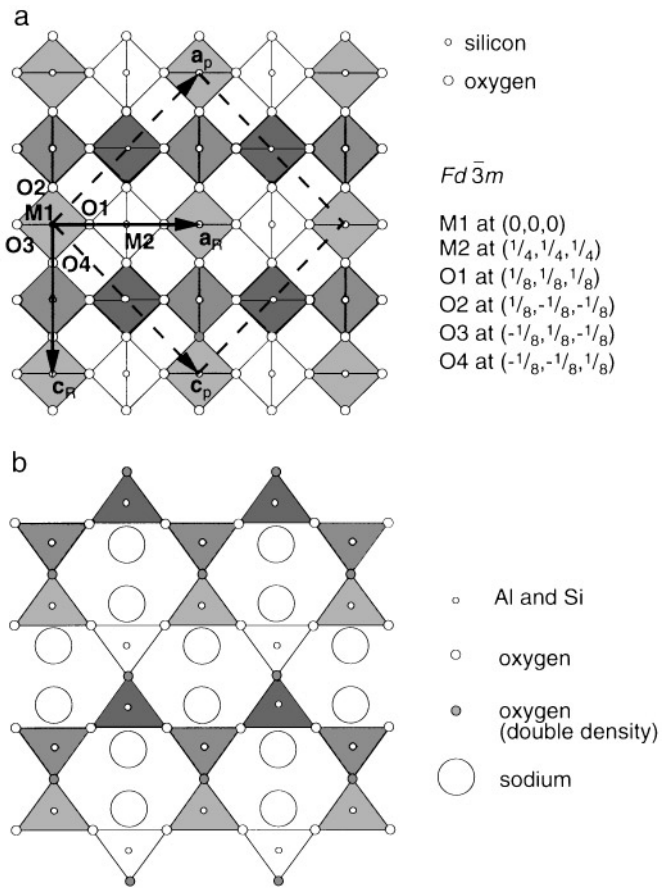

FIG. 1. (a) [010] projection of the idealized $Fd\bar{3}m$, SiO_2-cristobalite, or *C*9, structure type. $\mathbf{a}_R = \frac{1}{2}(\mathbf{a}_p + \mathbf{c}_p)$, $\mathbf{b}_R = \mathbf{b}_p$ and $\mathbf{c}_R = \frac{1}{2}(-\mathbf{a}_p + \mathbf{c}_p)$, where p corresponds to the *C*9 parent unit cell and R the resultant unit cell. (b) $\langle 101 \rangle$ projection of idealized "stuffed" *C*9 structure. Partial replacement of the Si^{4+} ions in such a framework structure by ions of lower valence such as Al^{3+} leads to so-called stuffed *C*9 structures in which charge balance is maintained by alkali metals such as Na occupying ideally 12 coordinate interstitial sites.

Leadbetter (4) and O'Keeffe and Hyde (3) proposed static microdomains of $I\bar{4}2d$ symmetry, while more recently, Hatch and Ghose (5) proposed dynamic microdomains of $P4_12_12$ symmetry. Both models involve short range ordered domains of a distorted *C*9 type framework which, on macroscopic averaging over all domain orientations, conforms with $Fd\bar{3}m$ space group symmetry. While these models have chemically plausible Si–O bond lengths and Si–O–Si angles there has never been any direct evidence for such disordered microdomain structures.

New insight into the structure of β-cristobalite followed the observation of a strong diffuse intensity distribution in electron diffraction patterns (EDPs) taken above the $\alpha \leftrightarrow \beta$ phase transition (6–8). These EDPs showed the existence of characteristic polarized sheets of diffuse intensity normal to each of the six $\langle 110 \rangle$ tetrahedral edge directions of the *C*9 average structure, corresponding in real space to $\langle 110 \rangle$ columns of atoms with motion strongly correlated along $\langle 110 \rangle$ but completely uncorrelated from one column to the next in directions perpendicular to that particular $\langle 110 \rangle$ direction.

Initial force model calculations (6) and more recent calculations in terms of rigid unit modes (RUMs) (9, 10) all showed that the diffuse intensity distribution observed for β-cristobalite was due to low-lying relatively dispersionless branches of the phonon dispersion curve diagrams. The motion of the rigid SiO_4 tetrahedral "units" corresponds to coupled rotations of strings of tetrahedra along $\langle 110 \rangle$ directions (Fig. 2), with the motion in neighboring columns being effectively uncoupled.

The electron diffraction data and force model calculations for β-cristobalite implied a dynamically disordered structure which, time- and space-averaged, has $Fd\bar{3}m$ symmetry. Direct evidence for a dynamically disordered structure is provided by variable-temperature solid state nuclear magnetic resonance (NMR) studies through the $\alpha \leftrightarrow \beta$ phase transitions in SiO_2-cristobalite and its $AlPO_4$ analogue (11), the presence of $Fd\bar{3}m$ symmetry-forbidden bands in the IR spectrum of β-cristobalite (12), the rapidity of the $\alpha \leftrightarrow \beta$ phase transition in TEM studies (7) and from molecular dynamics simulations and inelastic neutron scattering data (13, 14). Taken together with the absence of static micro-domains in medium resolution TEM images of β-cristobalite (7), the dynamically disordered model for β-cristobalite fits all available evidence to date.

Such a dynamically disordered structural model does not preclude that, instantaneously, small local regions might adopt $I\bar{4}2d$ or $P4_12_12$ symmetry as proposed by the above microdomain models (3–5). It rather suggests that these two

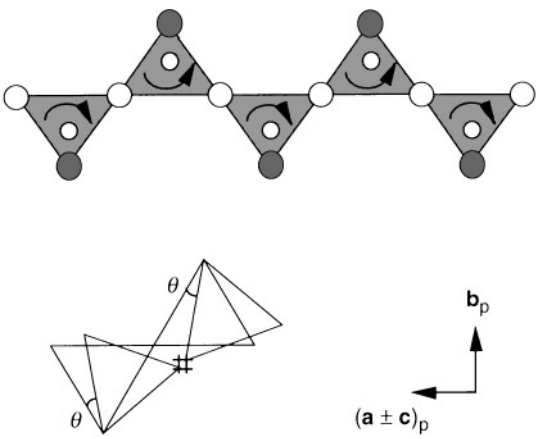

FIG. 2. Coupled rotation of the framework tetrahedra about their $\langle 101 \rangle_p$ tetrahedral edges is the natural "normal mode" for C9-related structures. Such rotation results in a contraction of the ideal unit cell dimensions along the orthogonal $[010]_p$ and $\langle 101 \rangle_p$ axes. The amount of this contraction depends upon the magnitude of the rotation angle θ.

particular microdomain possibilities are but two of a much wider range of equally plausible local configurations each of which could provide chemically plausible local structures. It should be kept in mind that NMR spectroscopic evidence mentioned above (11) requires a timescale for the existence of any such domains of less than 1 μs.

This improved understanding of the structure of β-cristobalite has provided insight into how best to describe cristobalite-related structures including those structure types discovered since the previous review (3). With only one exception they can be derived from a $C9$ type parent structure, where the parent structure has ideal M–O bond lengths for its composition, via concerted rotations of $\langle 110\rangle_p$ (p = parent) strings of tetrahedra about two mutually orthogonal $\langle 110\rangle_p$ axes. This concerted motion is the same sort of motion as that proposed for β-cristobalite. In β-cristobalite all possible rotation patterns occur. In each of the long range ordered, cristobalite-related structures, one such rotation pattern locks in.

We have provided such a description for low-carnegieite (15), $KGaO_2$-type, Na_2MgSiO_4-type, and γ-$NaAlO_2$-type (16) and for the new structure types at $x = 0.35$ and 0.7–0.9 in the system $Na_{2-x}Al_{2-x}Si_xO_4$, $0 \le x \le 1$ (17). As will be presented below such a description is equally applicable to the β-$NaAlO_2$-type (18), the other reported structure for Na_2MgSiO_4 (19) and indeed for the hypothetical $I\bar{4}2d$ structure of SiO_2, which is reported for β-$KCoO_2$ (20) and γ-$LiBO_2$ (21). In some of these cases there is also compositional ordering and subsequent structural relaxation associated with the occupancy of the interstitial sites and/or the tetrahedral framework cations.

The only exception to this simple derivation is the cubic phase at $x \approx 0.5$–0.6 in the system $Na_{2-x}Al_{2-x}Si_xO_4$, $0 \le x \le 1$, (17) which is anomalous in that its symmetry is incompatible with the above generic mechanism for collapsing the $C9$ structure type, namely, concerted rotation about two mutually orthogonal $\langle 110\rangle_p$ axes.

The first objective of this review is to represent and discuss known cristobalite-related oxide structures in terms of concerted rotations of $\langle 110\rangle_p$ strings of tetrahedra about two mutually orthogonal $\langle 110\rangle_p$ axes. The second objective is to identify trends in behavior in the distortion of these structures from their $C9$ parent structure. The third objective is to try to understand why one structure type is preferred over the others for any given chemical composition.

2. OBSERVED CRISTOBALITE-RELATED STRUCTURE TYPES

The review of cristobalite-related structures by O'Keeffe and Hyde (3) included all known cristobalite-related oxides to that time. Since then there have been many compounds added to that list.

As discussed earlier, all noncubic cristobalite-related structures can be derived from an appropriate $C9$ parent structure by concerted rotations of $\langle 110\rangle_p$ strings of tetrahedra about two mutually orthogonal $\langle 110\rangle_p$ axes. What characterises each structure is its pattern of rotations and any compositional ordering of interstitial and/or tetrahedral framework cations. Consequently these structures can be classified primarily according to their pattern of rotations and secondarily according to cation ordering.

Excluding the cubic structure at $x \approx 0.5$–0.6 in the system $Na_{2-x}Al_{2-x}Si_xO_4$, $0 \le x \le 1$, there are only seven unique patterns of rotation. These are β-$KCoO_2$-type, α-cristobalite-type, β-$NaFeO_2$-type, and $KGaO_2$-type, all of which exhibit many examples. There are two examples of the orthorhombic Na_2MgSiO_4 pattern and only one example each of the two remaining patterns, namely $x \approx 0.35$ and $x \approx 0.7$–0.9 in the system $Na_{2-x}Al_{2-x}Si_xO_4$.

Projecting these cristobalite-related structures down their $[010]_p$ (p = parent) axis enables direct observation of the different tetrahedral rotation patterns about both the relevant $\langle 101\rangle_p$ axes. Figure 3 shows polyhedral representations of the tetrahedral frameworks of refined structures exemplifying each of the different patterns of rotation. The " + " and " − " signs indicate the sense of rotation of each tetrahedral string. The significance of these patterns of rotation is discussed later.

These cristobalite-related structures can be further subdivided according to the compositional ordering of tetrahedral framework cations. Figure 3 also presents the tetrahedral frameworks of refined structures exemplifying each of the observed tetrahedral cation ordering patterns.

Also represented in Fig. 3 for comparison are equivalent projections for those structures with cubic symmetry. It is assumed that all structures with $Fd\bar{3}m$ and $F\bar{4}3m$ symmetry are to some extent displacively disordered in the manner of β-cristobalite, the difference between the two symmetries being that $F\bar{4}3m$ allows for tetrahedral framework cation ordering.

A full classification of all cristobalite-related oxide structures is given in Table 1 including the space groups, the relationships of the unit cells to their parent $C9$ structure and references (22–75) containing structural details and/or the unit cells.

An alternative description of β-$NaFeO_2$- and m-Na_2MgSiO_4-types (C) which is often cited is as würtzite-type where the alkali and framework cations occupy half the tetrahedral sites in a hexagonal close-packed oxygen array (76, 77). Such a description treats alkali oxide tetrahedra (e.g., LiO_4, NaO_4) and framework metal oxide tetrahedra (e.g., SiO_4, FeO_4) equally even though the strength of the bonding interactions within the two types of tetrahedra are very different. In contrast to our tetrahedal framework description, treating β-$NaFeO_2$- and m-Na_2MgSiO_4-types as hexagonal close-packed oxygen arrays fails to account for the

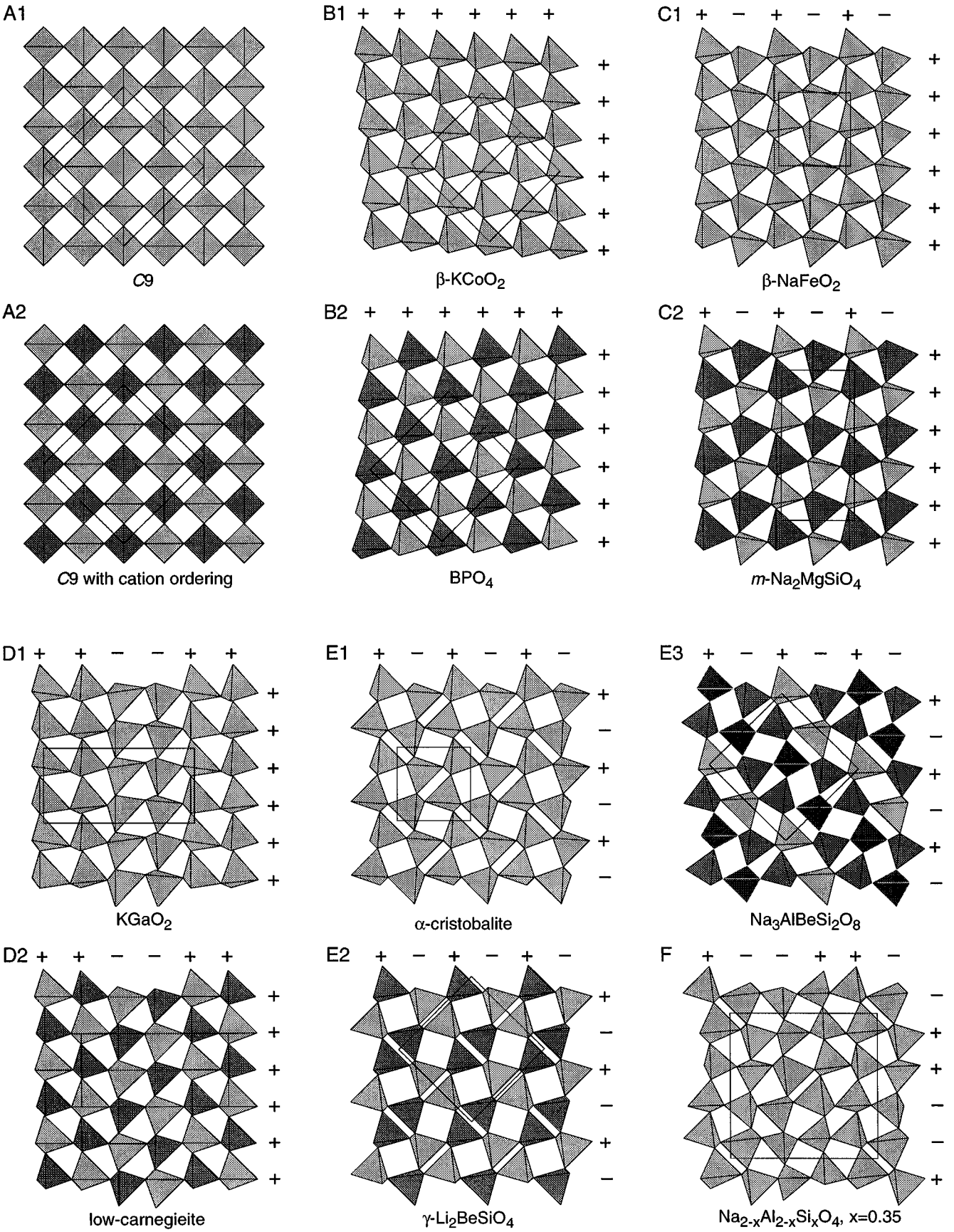
A1
C9
B1 + + + + + +
β-KCoO2
C1 + − + − + −
β-NaFeO2
A2
C9 with cation ordering
B2 + + + + + +
BPO4
C2 + − + − + −
m-Na2MgSiO4
D1 + + − − + +
KGaO2
E1 + − + − + −
α-cristobalite
E3 + − + − + −
Na3AlBeSi2O8
D2 + + − − + +
low-carnegieite
E2 + − + − + −
γ-Li2BeSiO4
F + − − + + −
Na2-xAl2-xSixO4, x=0.35

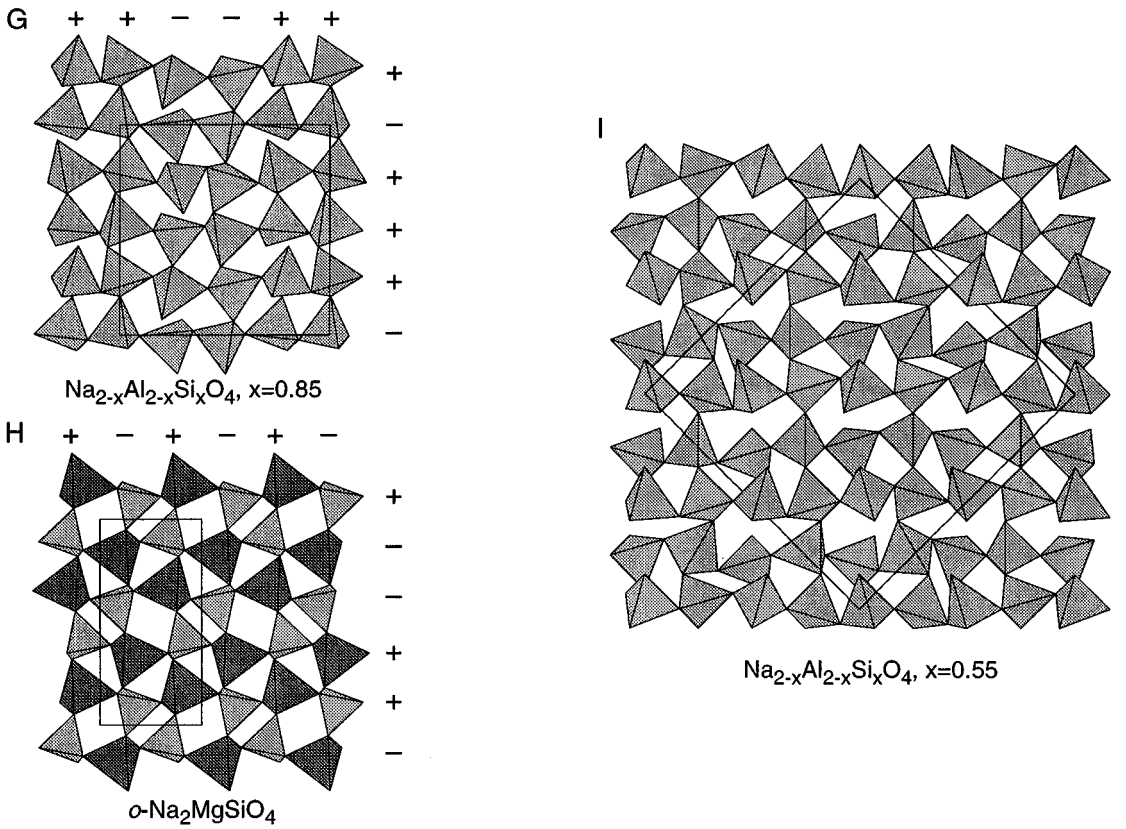

FIG. 3. Projection along the $[010]_p$ axis of the tetrahedral frameworks of various cristobalite-related structures showing their patterns of coupled tetrahedral edge rotation about the two orthogonal $\langle 101\rangle_p$ directions, except for *C*9 (A1 and A2) which are undistorted. Examples of each different pattern of rotation are given juxtaposed to related structures which display compositional ordering of tetrahedral framework cations. The "+" and "−" signs indicate the sense of rotation of each tetrahedral string. The labels for the structure types correspond to the categories in Table 1. Unit cell outlines are superimposed.

readily reversible phase transitions to higher symmetry cristobalite-related structures which occur at high temperatures for most of these phases, nor does it account for the alkali ion conductivity observed in most of the systems. Close packed oxygen arrays convey the impression of being rigid (e.g., hcp in α-Al_2O_3, ccp in MgO) whereas all the experimental evidence for this subset of cristobalite-related oxides is that their structures are inherently flexible and their interstitial cations relatively mobile. The framework description also has the advantage of allowing for a unifying description of structures within and between all the oxide systems covered by Table 1.

3. RECIPROCAL SPACE RELATIONSHIP OF STRUCTURES TO β-CRISTOBALITE

Cristobalite-related structures can also be related to β-cristobalite in reciprocal space. In electron diffraction patterns (EDPs) of β-cristobalite narrow polarized sheets of diffuse intensity are observed normal to the six $\langle 110\rangle$ directions of real space. This diffuse intensity distribution corresponds to $\langle 110\rangle$ columns of atoms whose motion is strongly correlated along $\langle 110\rangle$ but completely uncorrelated from one column to the next in directions perpendicular to the direction of motion. As can be seen in Fig. 2 the motion is predominantly along the $\langle 110\rangle$ column direction. In terms of a modulated structure description, the observed diffuse distribution corresponds to all possible modulation wavevectors normal to the $\langle 110\rangle$ directions being equally excited, which in real space implies that all possible patterns of concerted rotation of the $\langle 110\rangle$ tetrahedral strings are represented.

If EDPs of cristobalite-related derivative structures are compared with the corresponding EDPs for β-cristobalite, the coincidence of the $Fd\bar{3}m$ parent structure reflections is immediately apparent as is the fact that the strongest satellite, or superstructure, reflections always coincide with the same polarized sheets of diffuse intensity observed for β-cristobalite. Figure 4, for example, shows selected area EDPs for the $KGaO_2$-type $x = 0.45$, $Na_{2-x}Al_{2-x}Si_xO_4$,

TABLE 1
Classification of Cristobalite-Related Structures

	Structure type	Space group	Relation to parent structure	Formula/reference
A1	High-cristobalite type	$Fd\bar{3}m$	$a_R = a_p$	SiO_2 (22) $KFeO_2$ (23, 24) $KAlO_2$ (24, 25) $K_{1-x}Fe_{1-x}Ti_xO_2$, $0 < x \leq 0.20$ (24) $K_{1-x}Al_{1-x}Ti_xO_2$, $0 < x \leq 0.25$ (24) $K_{1-x}Al_{1-x}Si_xO_2$, $0 < x \leq 0.10$ (24)
A2	High-carnegieite type	$F\bar{4}3m$	$a_R = a_p$	$NaAlSiO_4$ (27) $AlPO_4$ (4) $GaPO_4$ (26) K_2MgSiO_4 (28) Na_2CaSiO_4 (29)[a] K_2BeSiO_4 (30) K_2MgGeO_4 (30) K_2CdSiO_4 (30) K_2CdGeO_4 (30) K_2ZnSiO_4 (30) K_2ZnGeO_4 (31)
B1	β-$KCoO_2$-type	$I\bar{4}2d$	$a_R = 1/\sqrt{2}a_p$ $b_R = b_p$ $c_R = 1/\sqrt{2}c_p$	β-$KCoO_2$ (20) Hypothetical $I\bar{4}2d$ SiO_2 (3) γ-$LiBO_2$ (21)
B2	BPO_4-type	$I\bar{4}$	$a_R = 1/\sqrt{2}a_p$ $b_R = b_p$ $c_R = 1/\sqrt{2}c_p$	BPO4 (33) BeSO4 (32) GaPO4 (34) BAsO4 (33) LiBGeO4 (35)
C1	β-$NaFeO_2$-type	$Pna2_1$	$a_R = 1/2a_p$ $b_R = b_p$ $c_R = 1/\sqrt{2}c_p$	β-$NaFeO_2$ (36) β-$NaAlO_2$ (18) β-$NaFeO_2$–$SiO_{2(ss)}$ (37) α-$NaGaO_2$ (38, 39) β-$LiGaO_2$ (40).
C2	m-Na_2MgSiO_4-type	Pn	$a_R = \sqrt{2}a_p$ $b_R = 2b_p$ $c_R = 1/\sqrt{2}c_p$ $\beta \approx 90^\circ$	Na_2MgSiO_4 (19) Na_2ZnSiO_4 (41, 42) Na_2ZnGeO_4 (41, 39, 43, 44, 45) Na_2MgGeO_4 (41) Ag_2ZnSiO_4 (46, 47) Ag_2ZnGeO_4 (46)
D1	$KGaO_2$-type	$Pbca$	$a_R = \sqrt{2}a_p$ $b_R = 2b_p$ $c_R = 1/\sqrt{2}c_p$	$KGaO_2$ (38, 48) $Na_{2-x}Al_{2-x}Si_xO_4$, $x = 0.25$ and $x = 0.45$ (49) $Na_{1.74}Mg_{0.79}Al_{0.15}Si_{1.06}O_4$ (16) $Na_4Mg_2Si_3O_{12}$ (50) γ'-$NaFeO_2$-$SiO_{2(ss)}$ (37) $RbGaO_2$ (38) $CsGaO_2$ (38) $RbFeO_2$ (51) $KFeO_2$ (52) $KAlO_2$ (52) Na_2ZnSiO_4 (53, 54) $Na_3MgAlSi_2O_8$ (55) $Na_{1.8}Be_{0.9}Si_{1.4}O_4$ (56) $Na_{1-x}Ga_{1-x}Ge_xO_2$, $x = 0.20$ and $x = 0.25$ (39) $Na_{0.90}Zn_{0.45}Ge_{0.55}O_2$ (39) $K_{0.90}Zn_{0.45}Ge_{0.55}O_2$ (48) $K_{0.9}Ga_{0.9}Ge_{0.1}O_2$ (48) $Na_{1.9}ZnSi_{0.9}P_{0.1}O_4$ (57) $Na_{2-2x}Be_{1-x}Si_{1+x}O_4$, $0.0 \leq x \leq 0.1$ (53) $Ag_{2x}Na_{2-2x}ZnSiO_4$, $0 \leq x \leq 1$ (47) $Na_{0.9}K_{0.1}Zn_{0.5}Ge_{0.5}O_2$ (39) $Na_{1.8}Be_{0.9}Si_{1.1}O_4$–$Na_{1.8}Zn_{0.9}Si_{1.1}O_4$ (58)

TABLE 1—*Continued*

D2	Low-carnegieite type	$Pb2_1a$	$a_R = \sqrt{2}a_p$ $b_R = 2b_p$ $c_R = 1/\sqrt{2}c_p$	$NaAlSiO_4$ (15) Na_2BeSiO_4 (59, 60, 61) K_2ZnGeO_4 (62, 31) K_2ZnSiO_4 (62), Rb_2ZnGeO_4 (62) $(Na_{1.4}K_{0.6})ZnGeO_4$ (63) $Na_{1.8}(Ga_{0.2}Zn_{0.8})SiO_4$ (60) $Na_{1.8}(Ga_{0.2}Zn_{0.8})GeO_4$ (60) Ag_2BeSiO_4 (46) K_2MgGeO_4 (64) K_2CdGeO_4 (64)
E1	α-Cristobalite-type	$P4_12_12$	$a_R = 1/\sqrt{2}a_p$ $b_R = 2b_p$ $c_R = 1/\sqrt{2}c_p$	SiO_2 (65) γ-$NaAlO_2$ (66) γ-$NaFeO_2$ (66) γ-$NaFeO_2$–$SiO_{2(ss)}$ (67) $Na_{2-x}Al_{2-x}Si_xO_4$, $x = 0.05$ (49) $Na_{1.8}Mg_{0.9}Si_{1.1}O_4$ (16) γ-$LiAlO_2$ (68, 69) GeO_2 (70)
E2	γ-Li_2BeSiO_4-type	$C222_1$	$a_R = a_p$ $b_R = b_p$ $c_R = c_p$	γ-Li_2BeSiO_4 (71) AlPO4 (72) GaPO4 (73)
E3	$Na_3AlBeSi_2O_8$	$P2_12_12$	$a_R = a_p$ $b_R = b_p$ $c_R = c_p$	$Na_3AlBeSi_2O_8$ (74)
F	$Na_{2-x}Al_{2-x}Si_xO_4$, $x = 0.35$	$P4_12_12$	$a_R = \sqrt{2}a_p$ $b_R = b_p$ $c_R = \sqrt{2}c_p$	$Na_{2-x}Al_{2-x}Si_xO_4$, $x = 0.35$ (49)
G	$Na_{2-x}Al_{2-x}Si_xO_4$, $x = 0.85$	$Pc2_1b$	$a_R = \sqrt{2}a_p$ $b_R = 2b_p$ $c_R = \sqrt{2}c_p$	$Na_{2-x}Al_{2-x}Si_xO_4$, $x = 0.85$ (49)
H	o-Na_2MgSiO_4	$Pna2_1$	$a_R = \sqrt{2}a_p$ $b_R = b_p$ $c_R = 1/\sqrt{2}c_p$	Na_2MgSiO_4 (16) Na_2ZnSiO_4 750°C (75)
I	$Na_{2-x}Al_{2-x}Si_xO_4$, $x = 0.55$	$P2_13$	$a_R = 2a_p$	$Na_{2-x}Al_{2-x}Si_xO_4$, $x = 0.55$ (49)

[a] Orientationally disordered.

structure juxtaposed to a schematic superposition of the same diffraction patterns with their equivalent zone axes from β-cristobalite. Figure 5 shows a similar juxtaposition for the tetragonal $x = 0.35$ structure from the same system.

Where strong satellite reflections occur which either do not fall on the β-cristobalite type diffuse distribution or which do fall on the diffuse but which do not exhibit the same characteristic polarized intensity distribution, it can safely be assumed that cation ordering and associated structural relaxation characterized by the relevant modulation wave-vector is responsible.

In $KGaO_2$-type structures the satellite reflections from the displacive modulations associated with the observed modulation wave-vectors, namely $\frac{1}{4}[020]^*_p$, $\frac{1}{4}[202]^*_p$, $\frac{1}{4}[222]^*_p$, and $\frac{1}{4}[\bar{2}2\bar{2}]^*_p$, all fall on the polarized sheets of diffuse intensity and arise purely as a result of correlated rotation of $\langle 110\rangle_p$ tetrahedral strings. For the $x = 0.35$ structure the strongest satellite reflections are associated with $\frac{1}{4}[220]^*_p$ and $\frac{1}{4}[\bar{2}20]^*_p$ modulation wave-vectors, which also fall on the sheets of diffuse intensity. For this latter structure, however, significant intensity is also observed in these satellite reflections close to the origin of reciprocal space which does not coincide with the diffuse intensity distribution characteristic of pure tetrahedral edge rotation. This observation and the presence of these satellite reflections in the [010] zone axis EDP implies that there is cation ordering as well as correlated rotation of $\langle 110\rangle_p$ tetrahedral strings associated with these particular modulation wave-vectors.

The specific phase relationships between the rotations of neighbouring $\langle 110\rangle_p$ tetrahedral strings are provided in such cases by the particular modulation wave-vectors

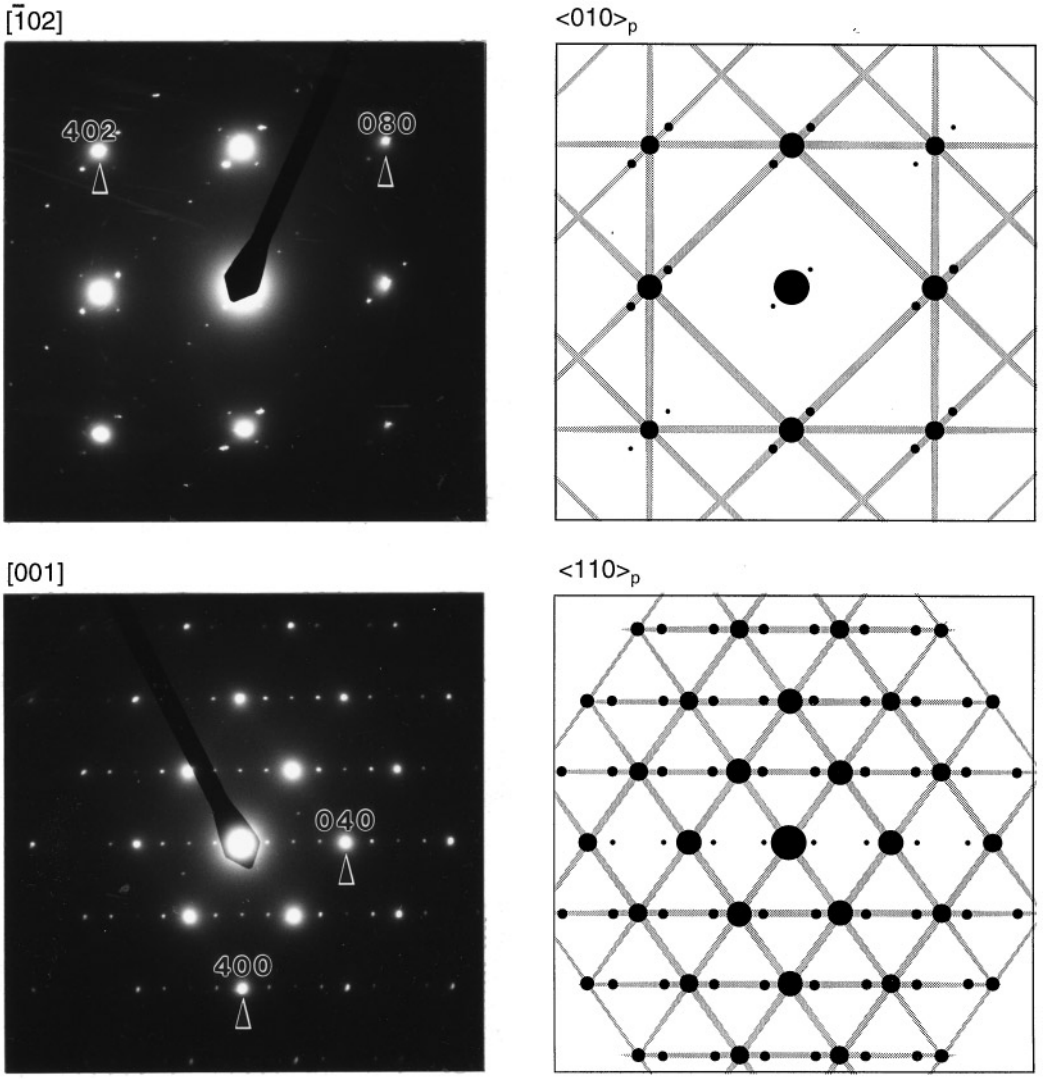

FIG. 4. Selected area EDPs of the $KGaO_2$-related phase with *Pbca* symmetry from the $Na_{2-x}Al_{2-x}Si_xO_4$ system at $x = 0.45$, juxtaposed to schematic superposition of the same diffraction patterns with their equivalent zone axis in β-cristobalite. The strong satellite, or superstructure, reflections coincide with the same sheets of diffuse intensity observed for β-cristobalite.

observed. Assuming that the magnitudes of rotation of neighboring strings are equal a unique rotation pattern, or at least a limited set of homometric possibilities, can then be generated.

The observed sheets of diffuse intensity characteristic of the reciprocal lattice of β-cristobalite suggest an effectively infinite number of distinct possible cristobalite-related derivative structures based on different patterns of $\langle 110 \rangle_p$ tetrahedral string rotations. If, however, we require that only two mutually orthogonal $\langle 110 \rangle_p$ tetrahedral edge rotation axes are allowed, then the number of resultant possibilities is significantly reduced. Furthermore, if the magnitudes of rotation of neighboring $\langle 110 \rangle_p$ strings are constrained to be equal, this number is reduced further still. These constraints may in fact be the reasons that only commensurately modulated, cristobalite-related derivative structures have so far been found. In this review we have limited our discussion to commensurate modulated structures or, as they are often known, superstructures.

4. DERIVATION OF POSSIBLE DISPLACEMENT PATTERNS

While there are an infinite number of possible patterns of $\langle 110 \rangle_p$ tetrahedral string rotation only seven relatively simple patterns are observed. What is common among the observed structures is that the two rotation angles θ_x, about $[101]_p$, and θ_z, about $[\bar{1}01]_p$, (axes with respect to Fig. 1)

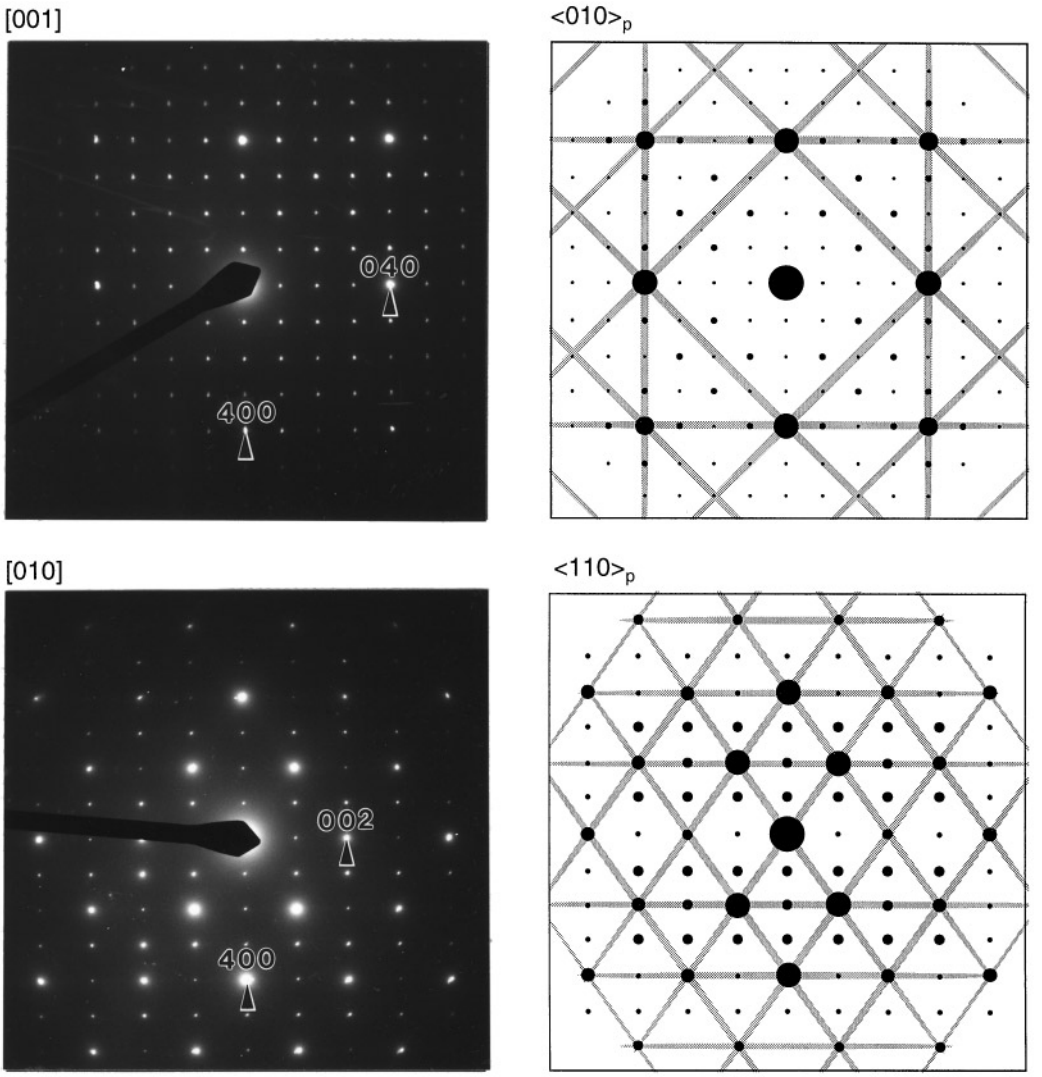

FIG. 5. Selected area EDPs of the $x = 0.35$ phase with $P4_12_12$ symmetry from the $Na_{2-x}Al_{2-x}Si_xO_4$ system, juxtaposed to schematic superposition of the same diffraction patterns with their equivalent zone axis in β-cristobalite. The strongest satellite reflections are associated with $\frac{1}{4}[220]^*_p$ and $\frac{1}{4}[\bar{2}20]^*_p$ modulation wave-vectors which coincide with the sheets of diffuse intensity. Unlike the $x = 0.45$ structure in Fig. 4 significant intensity is also observed in these satellite reflections close to the origin of reciprocal space which does not coincide with the diffuse intensity distribution characteristic of pure tetrahedral edge rotation and is attributed to cation ordering and associated structural relaxation.

are always of a similar magnitude. As discussed later in Section 9 the reason for this is the preference of each cristobalite-related structure to have similar $\angle M$–O–M's, where M is the tetrahedral metal cation.

If we consider the nondegenerate patterns of rotation about $[101]_p$ and $[\bar{1}01]_p$ for the unit cell $\frac{1}{2}(\mathbf{a}_p + \mathbf{c}_p) \times \mathbf{b}_p \times \frac{1}{2}(-\mathbf{a}_p + \mathbf{c}_p)$ (see Fig. 1) there are three patterns possible. These are shown schematically in the top row of Fig. 6. If we expand the unit cell to $(\mathbf{a}_p + \mathbf{c}_p) \times \mathbf{b}_p \times (-\mathbf{a}_p + \mathbf{c}_p)$ there are a further seven patterns and these can be seen in the bottom two rows. What is evident from Fig. 6 is that the top six structures, which are all the permutations that do not involve the more complex '$+++-$', are represented in known structures. Of the four possibilities with the more complex '$+++-$' motif, only one is represented in a known structure.

The $KGaO_2$-type and $Na_{2-x}Al_{2-x}Si_xO_4$, $x = 0.85$, structures differ from the others in that they comprise two ~ 7 Å parent $C9$ layers stacked along the projection direction of Fig. 6. The pattern of rotation of the second layer is shown for these two structures in a smaller font. The two layers are related by a 2_1 screw axis along $\mathbf{b}_p$. In fact, two-layer structures can be generated for all of these single-layer rotation patterns by application of a 2_1 screw or

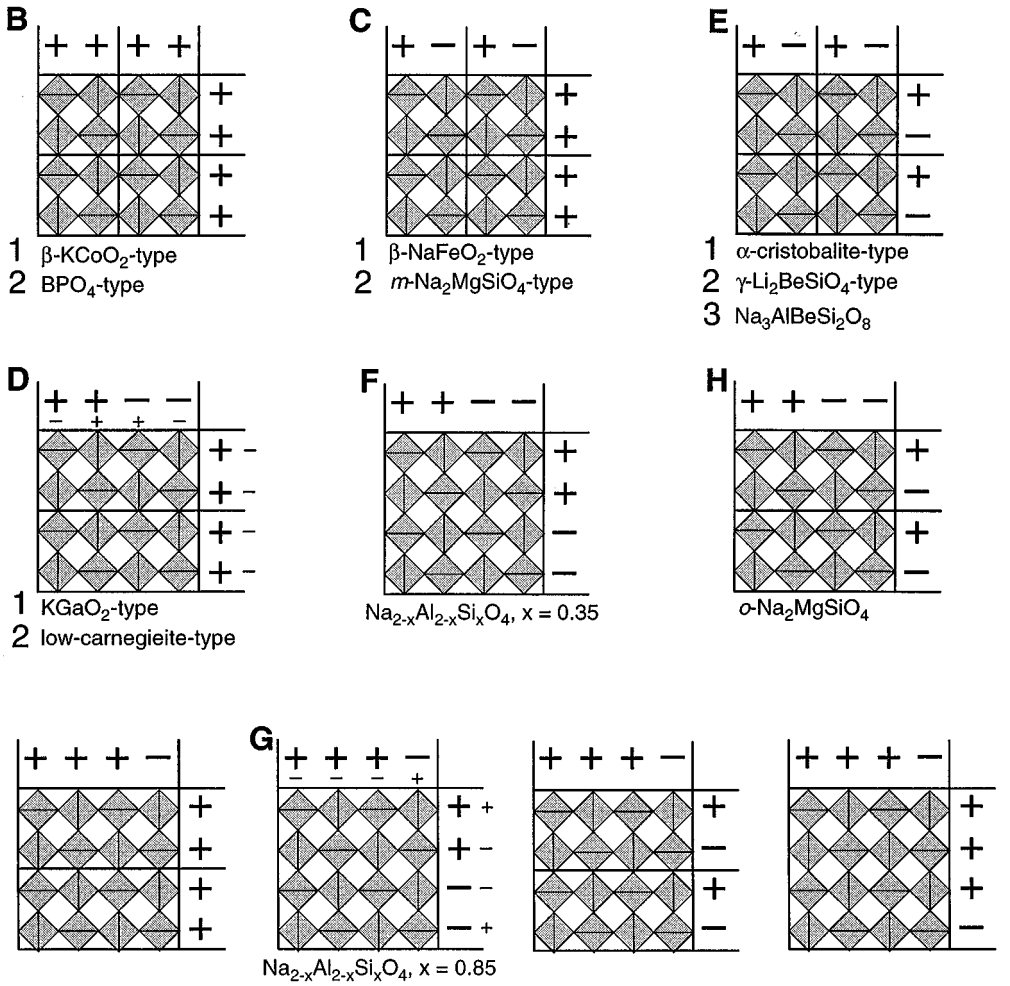

FIG. 6. Schematic representation of the three nondegenerate patterns of rotation about $[101]_p$ and $[10\bar{1}]_p$ for the unit cell $\frac{1}{2}(\mathbf{a}_p + \mathbf{c}_p) \times \mathbf{b}_p \times \frac{1}{2}(-\mathbf{a}_p + \mathbf{c}_p)$ (top row) and the further seven nondegenerate patterns for the unit cell to $(\mathbf{a}_p + \mathbf{c}_p) \times \mathbf{b}_p \times (-\mathbf{a}_p + \mathbf{c}_p)$ (bottom two rows). The top six patterns are all the permutations that do not involve the more complex "+ + + −" motif and are represented in known structures. Of the four possibilities with the more complex "+ + + −" motif, only one is represented in a known structure. The $KGaO_2$- and low-carnegieite types (D) and $Na_{2-x}Al_{2-x}Si_xO_4$, $x = 0.85$, (G) structures differ from the others in that they comprise two $\sim$7 Å parent *C*9 layers stacked along the projection direction with the pattern of rotation of the second layer indicated by the smaller font of "+" and "−".

translations such as $\frac{1}{2}\mathbf{a}_p + \mathbf{b}_p + \frac{1}{2}\mathbf{c}_p$, $\frac{1}{2}\mathbf{a}_p + \mathbf{b}_p - \frac{1}{2}\mathbf{c}_p$, and $\mathbf{a}_p + \mathbf{b}_p$ which do not map the pattern into itself. What characterizes these operations are that they all map the parent *C*9 structure into itself. Single-layer structures with the rotation patterns of $KGaO_2$-type (D1) and $x = 0.85$ (G) structures are also possible. In some cases swapping the signs in the pattern of rotations along one axis generates the enantiomorph, e.g., α-cristobalite-type (E1) changes from $P4_12_12$ to $P4_32_12$.

This idealized description of the noncubic cristobalite-related structures requires first that the tetrahedra are rigid, i.e., they remain regular upon distortion from the *C*9 parent, and second that rotation occurs only about the $[101]_p$ and $[\bar{1}01]_p$ axes. How well the actual structures fit these idealised models is treated more generally later, but inspection of the refined tetrahedral frameworks exemplified in Fig. 3 illustrates how some structures behave almost ideally, e.g., low-carnegieite (D2), whereas some show significant deviations, e.g., $KGaO_2$ (D1). In all cases idealized structures have coplanar tetrahedral edges which appear as discontinuous straight lines in the projection of Fig. 3.

5. COMPOSITIONAL ORDERING

For all of the patterns of rotation generated in Section 4 it is possible to generate further structures by compositional ordering of the tetrahedral framework cations. Ordering may involve two or more elements, and may be complete or

partial. Figure 3 presents example structures where tetrahedral cation ordering has been observed. In most cases where ordering is observed we see perfect ordering of two cation types, $M = A$ and B, such that each AO_4 tetrahedron shares vertices with four BO_4 and vice versa, e.g., BPO_4, the two Na_2MgSiO_4 structures, low-carnegieite and γ-Li_2BeSiO_4. $Na_3AlBeSi_2O_8$ shows more complicated yet perfect ordering whereas the $x = 0.35$ structure in the $Na_{2-x}Al_{2-x}Si_xO_4$ system shows partial Si : Al ordering among its three tetrahedral cation sites (17).

The only other structure reportedly displaying partial cation ordering was the $KGaO_2$-type structure observed in the $NaFeO_2$-SiO_2 system by Grey *et al.* (37). The $KGaO_2$-type structure has two symmetry inequivalent sites and these authors observed partial ordering of Fe and Si cations between the two sites. Unlike the perfectly ordered structures above, in $KGaO_2$-type each AO_4 tetrahedron shares vertices with two BO_4 and two AO_4 tetrahedra and vice versa.

Obviously there is, in principle, no limit to the number of possible arrangements of different tetrahedral cations that might give new structures. However, in practice, the most common is that which gives perfect alternation of A and B cations for an ABO_4 framework composition. The crystal chemical reason for this is simple. As the coordination of oxygen atoms in the framework is effectively twofold, and that of the cations necessarily fourfold, if the bonding requirements of the oxygens are to be satisfied then they must be bonded to two cations which most fully satisfy their bonding requirements. In the stuffed cristobalite-type structures, such as low-carnegieite, interstitial sodiums make up the deficit. Because the interstitial cations in stuffed cristobalites are in high coordination and are typically alkali metals which are monovalent, the bonding contribution of the interstitial cations to the framework oxygens will always be relatively small.

For cristobalite-related structures where perfect A : B ordering occurs it is more appropriate to consider a $C9$ type structure with $F\bar{4}3m$ symmetry, which incorporates such ordering (A2 in Fig. 3), as the parent structure. In general, compositional ordering lowers symmetry or generates a superstructure unless such ordering is allowed by the space group of the unordered structure type, e.g., $KGaO_2$-type and the $x = 0.35$ structure.

Finally, while this review deals almost exclusively with the structure and composition of the tetrahedral framework, compositional ordering is also possible in stuffed cristobalite structures where there is incomplete occupancy of the interstitial sites. However, interstitial cation/vacancy ordering tends to adopt the symmetry of the framework cation ordering, e.g., low-carnegieite and $Na_3AlBeSi_2O_8$, which is not surprising given that the interstitial cations provide charge balance for those tetrahedra containing trivalent and divalent cations.

6. $\langle 110\rangle_p$ TETRAHEDRAL STRING vs $\bar{4}$ AXIS ROTATION

The present review of cristobalite-related oxides describes all known noncubic cristobalite-related structures in terms of concerted rotations of $\langle 110\rangle_p$ strings of tetrahedra about two mutually orthogonal $\langle 110\rangle_p$ axes. By contrast, O'Keeffe and Hyde (3) in their review described three of the then known structure types in terms of concerted rotations of tetrahedra about their $\bar{4}$ axes. Are these two descriptions equivalent? If so, what are the relative merits of each?

The two descriptions can be considered equivalent when the two rotation angles in our $\langle 110\rangle_p$ tetrahedral string description are equal. The $\bar{4}$ rotation angle ϕ of O'Keeffe and Hyde (3) is related to our tetrahedral edge rotation angle θ by the relationship:

$$1/\sqrt{2}\tan\phi = \sin\theta\sqrt{(1 + 2\tan^2\theta)}.$$

To a very good approximation this gives $\phi = \sqrt{2}\theta$. The equivalence of the two descriptions is illustrated in Fig. 7, where $[010]_p$ projections of the tetrahedral frameworks of the hypothetical $I\bar{4}2d$ symmetry model for β-cristobalite

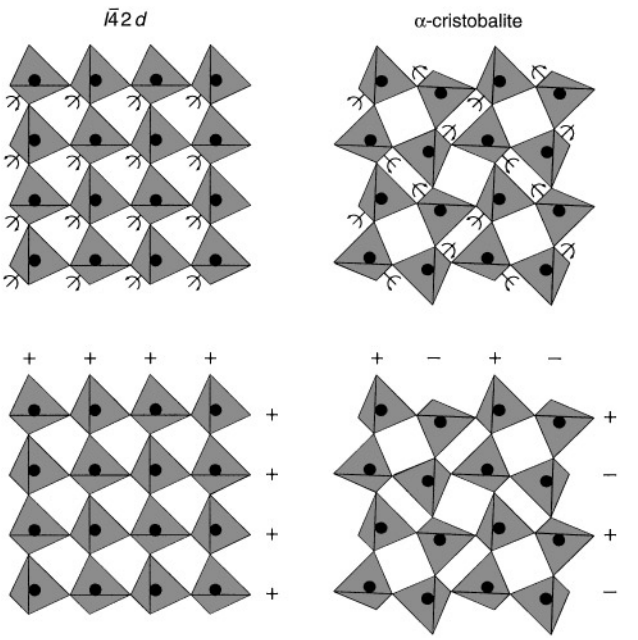

FIG. 7. $[010]_p$ projections of the tetrahedral frameworks of the hypothetical $I\bar{4}2d$ symmetry model for β-cristobalite (3) and the refined structure of low-cristobalite (65). The upper drawings are in terms of concerted rotations of tetrahedra about their $\bar{4}$ axes, corresponding to Sequences (I) and (II), respectively, of O'Keeffe and Hyde (3). In this projection the $\bar{4}$ rotation axes are all normal to the projection axis. The lower drawings show the same structures in terms of concerted rotations of $\langle 110\rangle_p$ strings of tetrahedra about two mutually orthogonal $\langle 110\rangle_p$ axes, as in Fig. 3.

and the refined structure of low-cristobalite are described in both ways. These two structures correspond to Sequences (I) and (II), respectively, of O'Keeffe and Hyde (3). In this projection the $\bar{4}$ rotation axes are all normal to the projection axis.

Figure 7 seems to show that, for any individual tetrahedron, rotation about a $\bar{4}$ axis is equivalent to equal rotation about two orthogonal $\langle 110\rangle_p$ axes, i.e., about two orthogonal tetrahedral edges. In other words rotation about a $\bar{4}$ axis is the sum of the two equal $\langle 110\rangle_p$ axis rotations. However, the two descriptions are only equivalent if one ignores the shift of origin required to map one into the other.

In the description of O'Keeffe and Hyde (3) the $\bar{4}$ rotation axis passes through the metal at the centre. Rotation about this axis leaves the metal position invariant while all four oxygen atoms are displaced. In our description, rotation of $\langle 110\rangle_p$ strings of tetrahedra about two orthogonal $\langle 110\rangle_p$ axes results in all the atoms being displaced. With the exception of the hypothetical $I\bar{4}2d$ symmetry model for β-cristobalite, where the space group requires that the metal atoms remain on the parent $C9$ positions, the tetrahedral metal atoms, M, in all noncubic cristobalite-related structures are displaced from their parent positions. Sequences (II) and (III) not only require rotation about two, noncollinear $\bar{4}$ axes, but they require four and two, respectively, different origins to generate their tetrahedral frameworks. Our tetrahedral edge rotation description is significantly simpler in that the resultant framework necessarily has a single origin.

A further disadvantage of the $\bar{4}$ rotation axis description is the constraint that all derivative structures must be metrically tetragonal. The authors finessed this difficulty for the orthorhombic Sequence (III) structures by introducing additional small $\bar{4}$ axis rotations, making their description remarkably complicated. The limitations of this description of cristobalite-related structures were further highlighted by the inability to describe the $KGaO_2$-type structure due to its complexity.

Except for the $I\bar{4}2d$ and $I\bar{4}$ structures (B in Figs. 3 and 6), which are more elegantly described in terms of concerted rotations of tetrahedra about their $\bar{4}$ axes (the special case where the two rotation angles θ_x and θ_z are equal and all tetrahedral strings rotate in the same direction), all other noncubic structures are best described in terms of concerted rotations of $\langle 110\rangle_p$ strings of tetrahedra about two mutually orthogonal $\langle 110\rangle_p$ axes. This follows from the close relationship between the dynamically disordered model for β-cristobalite and our description of cristobalite-related structures in that the lowest energy phonon modes in β-cristobalite all correspond to concerted tetrahedral edge rotation modes. The observed cristobalite-related structures can be considered as locked-in structures where the frequency of specific modes has dropped to zero.

7. OBSERVED COLLAPSE OF CRISTOBALITE-RELATED STRUCTURES

The collapse of the unit cell for all of the ideal cristobalite-related structures derived in Section 4 is directly related to the rotation angle θ. If we assume equal rotation about $[101]_p$ and $[10\bar{1}]_p$ for the unit cell $\frac{1}{2}(\mathbf{a}_p + \mathbf{c}_p) \times \mathbf{b}_p \times \frac{1}{2}(-\mathbf{a}_p + \mathbf{c}_p)$, where $a_p = (8/\sqrt{3})\ d_{M-O}$ the ideal average bond length, then the magnitude of the $\mathbf{a}_R$, $\mathbf{b}_R$, and $\mathbf{c}_R$ axes (R = resultant structure) are as follows:

$$a_R = c_R = a_p(1/\sqrt{2})\cos\theta,$$

$$b_R = a_p/\sqrt{(1 + 2\tan^2\theta)}.$$

Figure 8 plots the relative collapse of the a_R and b_R dimensions as a function of θ. Doubling of one or more of the axes of the structure simply multiplies through in these formulae and makes no difference to the relative collapse for a given θ. If rotations about the $[101]_p$ axis of θ_x and $[\bar{1}01]_p$ axis of θ_z are unequal then the equations become:

$$a_R = a_p(1/\sqrt{2})\cos\theta_z,$$

$$c_R = a_p(1/\sqrt{2})\cos\theta_x,$$

$$b_R = a_p/\sqrt{(1 + \tan^2\theta_z + \tan^2\theta_x)}.$$

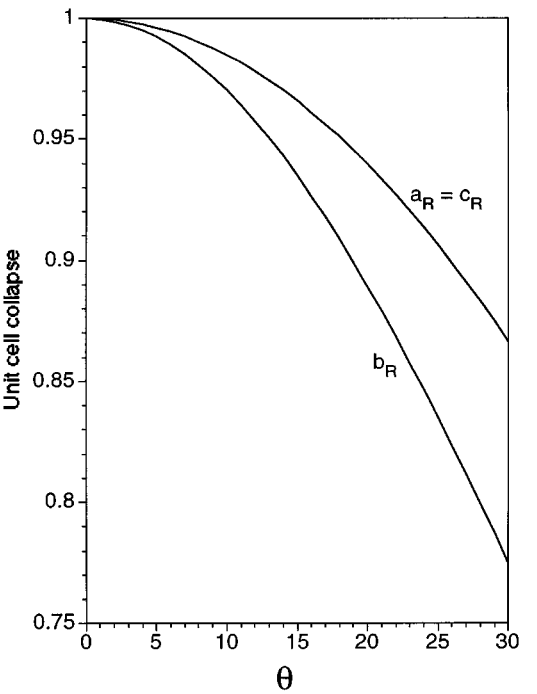

FIG. 8. Plot of the relative collapse of the a_R and b_R dimensions of collapsed $C9$ structure as a function of θ, where $a_R = c_R = a_p\,(1/\sqrt{2})\cos\theta$ and $b_R = a_p/\sqrt{(1 + 2\tan^2\theta)}$.

For example, in o-Na_2MgSiO_4, $Pc2_1n$, $a = 5.279(12)$ Å, $b = 7.067(8)$ Å, $c = 10.835(5)$ Å (16), which has $a_p = 8.251$ Å, rotation angles $\theta_x = 21.8^\circ$ and $\theta_z = 25.2^\circ$ are derived from the observed unit cell dimensions. Note that the structure of o-Na_2MgSiO_4 has been reset from its reported space group $Pna2_1$ to be consistent with the above general equations. Using these rotation angles a b dimension of 7.021 Å is predicted, compared with the observed 7.067(8) Å, a discrepancy of $\sim$0.7%. This good agreement between the predicted and observed axial ratios requires that o-Na_2MgSiO_4 comprises close to ideal MgO_4 and SiO_4 tetrahedra and that the distortion of the structure from its $C9$ parent involves only concerted rotation of $[10\bar{1}]_p$ and $[101]_p$ tetrahedral strings about $[101]_p$ and $[\bar{1}01]_p$, respectively. Both these features can be seen in the projection of the tetrahedral framework of o-Na_2MgSiO_4 down [010] in Fig. 3 (H).

Based on knowledge of the composition and unit cell dimensions alone it is possible to derive a relative collapse for each of the three dimensions for all known cristobalite-related oxides. Figure 9 plots these data as a function of the mean d_{M-O} for each structure as derived from the bond length-bond valence relationship (78, 79). Note that for all the phases the unit cells and space groups have been reset to be consistent with the definitions of $\mathbf{a}_R$, $\mathbf{b}_R$, and $\mathbf{c}_R$ given above. The axial setting for each structure type is given in Table 1.

What is evident from Fig. 9 is that there tends to be an increase in the collapse of the framework as the size of the tetrahedral framework increases. This trend can be seen more easily if we segment the data according to the composition of the interstices. The trend is most evident for the Na-containing phases (Fig. 9), which are the most numerous. The three Ag-containing phases are included with Na because of their very similar ionic radii.

Within the Na data we can also see the relatively ideal behavior of Na-containing phases in that the b dimension (as defined above) collapses more than the a and c dimensions. Similar behaviour is not generally observed when the interstices are unoccupied or occupied by the larger alkali cations (Fig. 9).

A breakdown of the Na containing structures according to structure type (Fig. 10) shows interesting detail. The α-cristobalite-type (E1) and $Na_3AlBeSi_2O_8$ (E3) and β-$NaFeO_2$- (C2) and m-Na_2MgSiO_4-types (C2) show ideal collapse behavior according to the equations given above, whereas the $KGaO_2$- (D1) and low-carnegieite-types (D2) and other structure-types (A, F, G, and I) do not. The two o-Na_2MgSiO_4-type structures (H) show close to ideal behavior. The top two plots in Fig. 10 show lines of best fit for the resultant a and c dimensions, corresponding to the respective rotation angles θ_z and θ_x, with the bottom line being the calculated collapse of the b_R dimension according to

$$b_R = a_p/\sqrt{(1 + \tan^2\theta_z + \tan^2\theta_x)}.$$

The ideal behavior of the α-cristobalite-type (E1) and β-$NaFeO_2$- (C1) and m-Na_2MgSiO_4-type (C2) structures and the almost ideal behavior of the two o-Na_2MgSiO_4-type structures (H) appear to correlate with these phases being fully stuffed, i.e., all the interstitial sites are filled with sodium ions. Conversely, most of the $KGaO_2$- and low-carnegieite-types and other structure-types are only partially stuffed. This correlation, together with the observation that cristobalite-related oxide structures with empty or Li-, K-, Rb-, or Cs-filled interstices behave nonideally, suggests that ideal collapse behavior is principally a function of the composition of the interstices rather than the rigidity of the tetrahedra in the framework. If the interstitial cations are too small (Li) or too big (K, Rb, Cs), or the interstices are only partially occupied by Na, the framework distorts to satisfy simultaneously the bonding requirements of both the tetrahedral and the interstitial cations.

The empirical evidence suggests that sodium is the most suitably sized of the alkali cations to occupy the interstices of an ideal collapsed $C9$ framework. This is so for a wide range of framework sizes, from BeSi to ZnGe. When the interstices are fully occupied by sodium the balance of bonding and nonbonding interactions is able to preserve the regularity of the tetrahedra even though intratetrahedral oxygen–oxygen distances in most cases (AlO_4, MgO_4, FeO_4, ZnO_4) are long enough to allow for some distortion. In other words the occurrence of regular tetrahedra in cristobalite-related oxides is not solely due to their intrinsic rigidity. Further evidence is provided for this in the next section.

An alternative explanation for the ideal or close-to-ideal behavior of the Na-containing α-cristobalite-type (E1), β-$NaFeO_2$-type (C1), m-Na_2MgSiO_4-type (C2), and o-Na_2MgSiO_4-type (H) structures might be that they all comprise a single $\sim$7 Å parent $C9$ layer whereas $KGaO_2$-type (D1), low-carnegieite-type (D2), and $Na_{2-x}Al_{2-x}Si_xO_4$, $x = 0.85$ (G), all comprise double $\sim$7 Å parent $C9$ layers which are related by a 2_1 screw axis along b_p. The only other relevant structure is $Na_{2-x}Al_{2-x}Si_xO_4$, $x = 0.35$ (F), which comprises a single $\sim$7 Å parent $C9$ layer and behaves nonideally. However, if structure type was the main determinant of ideal collapse behavior, then one would expect the unstuffed and Li-stuffed α-cristobalite-type (E1), γ-Li_2BeSiO_4 (E2), and β-$LiGaO_2$ (C1) structures to behave ideally and they do not.

What determines the degree of collapse is another important issue. In the case of unstuffed cristobalite-type oxides one would expect the $C9$ framework to collapse until nonbonding interactions became significant. These interactions could be oxygen–oxygen contacts or, as proposed by O'Keeffe and Hyde (80), cation–cation contacts. Inspection of refined structures, both unstuffed and stuffed, shows that, in all but the smallest frameworks, oxygen–oxygen distances are too large to be significant in limiting framework

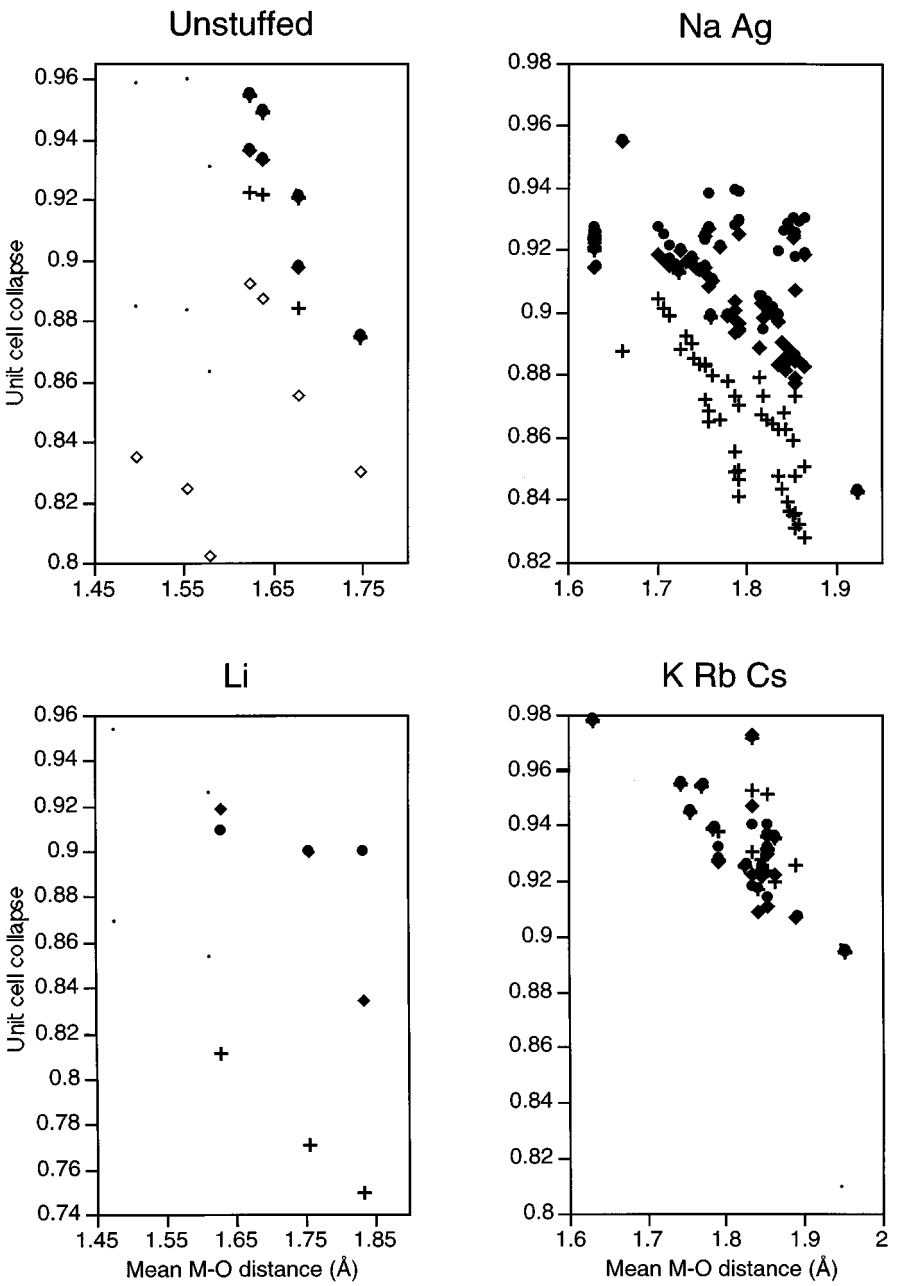

FIG. 9. Relative collapse for each of the three dimensions for all known cristobalite-related oxides as a function of the mean d_{M-O} for each structure as derived from the bond length-bond valence relationship (79, 80). Data are partitioned according to the contents of the interstices. Key: a_R (●), b_R (+), c_R (◆), $I\bar{4}2d$, and $I\bar{4}$ structure data (·), expected collapse of unstuffed structures based on nonbonded radii of O'Keeffe and Hyde (80) (◇).

collapse. Therefore, we should consider whether cation–cation contacts are a possible cause.

It is possible to derive the relative collapse of a tetrahedral framework which would bring the two tetrahedral cations into contact using the nonbonded radii R of O'Keeffe and Hyde (80). To do this we assume ideal tetrahedra and equal rotation about $[101]_p$ and $[\bar{1}01]_p$, i.e., $\theta_x = \theta_z$. We then derive $\angle M$–O–M from the two d_{M-O}s and the d_{M-M} derived from the nonbonded radii R of O'Keeffe and Hyde (80). From this we can calculate the collapse of the $C9$ framework along b_p by the approximation $\angle M$–O–$M \approx 180^\circ - 2\theta$.

For unstuffed structures in Fig. 9 we have also plotted the expected collapse along b_p based on these nonbonded radii,

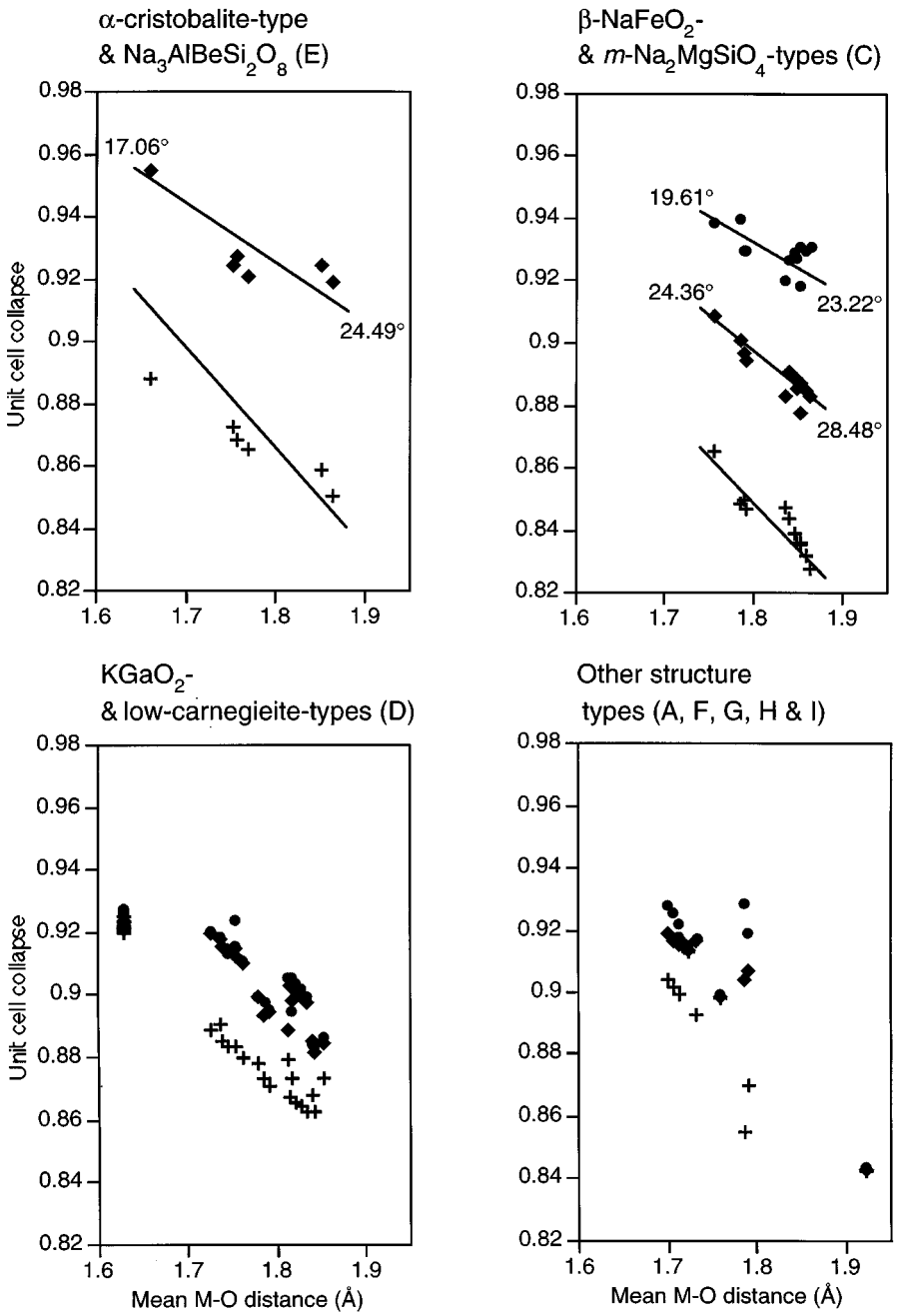

FIG. 10. Breakdown of the Na-containing structures according to structure type. The α-cristobalite-type and $Na_3AlBeSi_2O_8$ (E), and β-$NaFeO_2$- and *m*-Na_2MgSiO_4-types (C) show ideal collapse behavior according to the equations given above, whereas the $KGaO_2$-type and low-carnegieite type (D) and other structure types (A, F, G, H, and I) do not. Lines of best fit for the resultant *a* and *c* dimensions are shown, corresponding to the respective rotation angles θ_z and θ_x, with the bottom line being the calculated collapse of the b_R dimension such that $b_R = a_p/\sqrt{(1 + \tan^2\theta_x + \tan^2\theta_z)}$. Key: a_R (●), b_R (+), c_R (◆).

represented as open diamonds. As can be seen, the actual collapse along b_p (+) is significantly less than that required to bring the tetrahedral cations into contact as defined by O'Keeffe and Hyde (80). This is also the case for most of the stuffed cristobalite-related oxides. However, as these calculations assume inter alia ideal tetrahedra, a fairer assessment of the role of cation–cation contacts is provided in the next section, which examines the observed cation–cation distances in those cristobalite-related oxides for which the crystal structures have been refined.

8. CORRELATION OF STRUCTURAL PARAMETERS WITH COMPOSITION AND STRUCTURE TYPE

It follows from the previous section that those structures which display nonideal collapse behavior must consequently comprise nonideal tetrahedra. Of the 87 phases listed in Table 1 for which unit cell data are reported some 41 have refined atomic parameters. Note that some solid solutions have multiple structures reported at different compositions but only one is counted. One useful measure of the regularity of a tetrahedron is to calculate the standard deviation of its six $\angle$O–M–O angles. For an ideal tetrahedron this will be zero and, assuming plausible M–O bond lengths, the greater the standard deviation the more distorted is the tetrahedron.

Figure 11 plots the standard deviation of observed $\angle$O–M–O angles for each tetrahedron as a function of the ideality of the tetrahedral framework collapse for that structure. The latter is expressed as a ratio of the observed collapse along b_R and the expected collapse derived from the collapse along a_R and c_R. The data in Fig. 11 show a clear correlation between tetrahedral framework collapse and tetrahedron regularity. In particular the Na-containing α-cristobalite-type (E1) and $Na_3AlBeSi_2O_8$ (E3) and β-$NaFeO_2$- (C1) and m-Na_2MgSiO_4-types (C2) (●), which we have seen in the previous section as possessing relatively ideal collapse behavior, all have low standard deviations whereas all $KGaO_2$- (D1) and low carnegieite-type (D2) (◆ Na, ◇ K) do not and show increasingly nonideal collapse with increasing distortion of the tetrahedra. Of the former category, the three outliers are $Na_3AlBeSi_2O_8$, Na_2ZnGeO_4, and α-$NaGaO_2$. The first of these structures is unlike the others in that the interstitial sites are only $\frac{3}{4}$ filled by Na (refer to discussion in Section 7), the second displays extremely distorted tetrahedra and the structure model for the third contains a questionable oxygen positional parameter. Otherwise there is excellent correlation between the regularity of the tetrahedra and ideal behaviour of unit cell collapse from the $C9$ parent for these two classes of structures.

The remaining outliers belong to the unstuffed structures and $I\bar{4}2d$ structures (+) and the two Ag-containing structures (×). We have no explanation for the nonideal behavior of the unstuffed structures, which is even more puzzling in view of the absence of bonding interactions with interstitial cations. Of the two $I\bar{4}2d$ structures, β-$KCoO_2$ (20) and γ-$LiBO_2$ (21), the former might be expected to distort significantly due to its interstitial sites being fully occupied by the large K^+ cations, while the latter appears to behave similarly to the unstuffed structures.

What is striking about the Na-containing α-cristobalite-type (E1), β-$NaFeO_2$-type (C1), and m-Na_2MgSiO_4-type (C2) data is that most of the ideally behaved structures

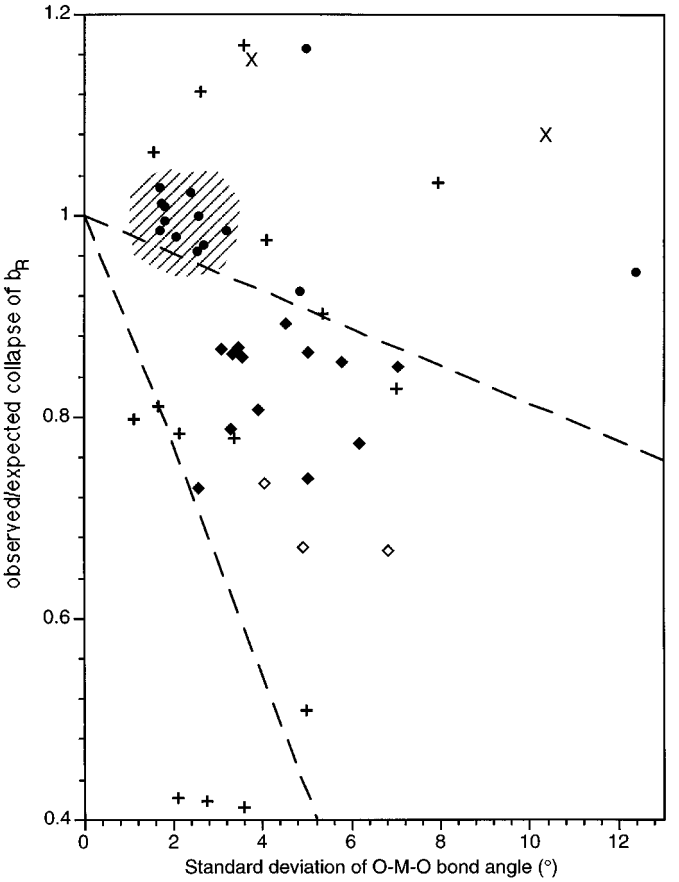

FIG. 11. Plot of the standard deviation of the $\angle$O–M–O angles for all refined cristobalite-related oxide structures as a function of the ideality of the tetrahedral framework collapse. The latter is expressed as a ratio of the observed collapse along b_R and the expected collapse derived from the collapse along a_R and c_R. The shaded region spans most of the Na stuffed α-cristobalite- (E1), β-$NaFeO_2$- (C1), and m-Na_2MgSiO_4-types (C2) (●). The dashed lines delineate the $KGaO_2$-type (D1) and low-carnegieite type (D2) (◆ Na, ◇ K). Unstuffed, $I\bar{4}2d$ (B1), F, G, and H structures are represented by + and the two Ag-containing structures by ×.

comprise tetrahedral framework cations (Mg, Al, Fe, Zn) which are not normally associated with regular tetrahedra.

Another useful correlation we have investigated from reported crystal structures is between the average framework size, represented as the mean d_{M-O}, and the mean $\angle$$M$–O–$M$ angle, seen in Fig. 12. Different symbols are used to indicate different interstitial cations. For each different interstitial cation we see a trend showing decreasing mean $\angle$$M$–O–$M$ angle with increasing mean d_{M-O}, most evident for Na-containing structures. The inverse correlation suggests that cation–cation contacts (80) might be limiting the collapse of the tetrahedral framework, however, the dependence of the mean $\angle$$M$–O–$M$ angle upon size of the interstitial cation indicates otherwise. A better explanation is that the tetrahedral frameworks collapse until the bonding requirements of the interstitial cations are satisfied.

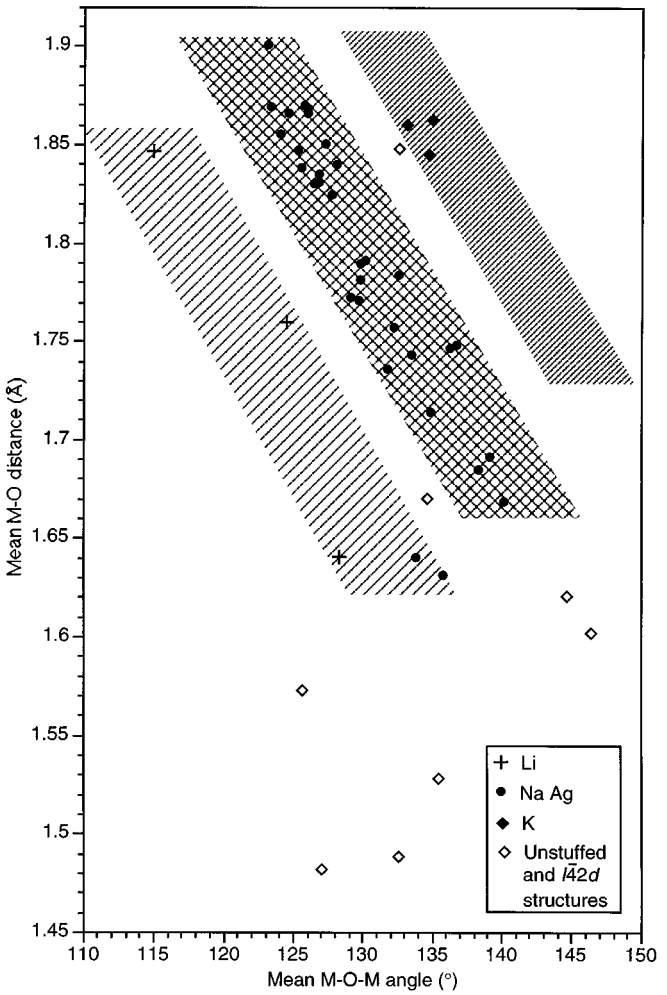

FIG. 12. Plot of the average framework size, represented as the mean d_{M-O}, vs the mean $\angle M$–O–M angle for all refined cristobalite-related oxide structures. The shaded areas delineate the different stuffing cations, Li^+, Na^+/Ag^+, and K^+.

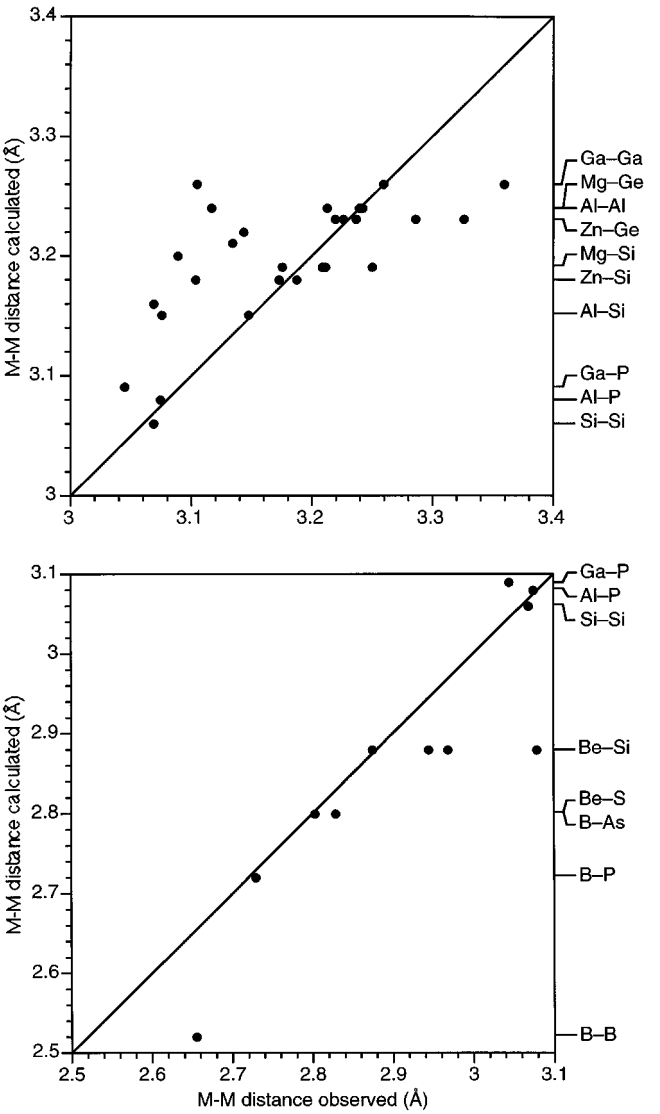

FIG. 13. Plot of observed vs calculated closest M–M distances where the calculated distances are the sums of the two nonbonded radii, R, published by O'Keeffe and Hyde (80). The data are limited to those structures for which nonbonded radii are available.

For any given interstitial cation the collapse is greater or less depending on whether the mean d_{M-O} is greater or less, respectively.

A final structural comparison is a plot of observed vs calculated closest M–M distances (Fig. 13) where the calculated distances are the sums of the two nonbonded radii, R, published by O'Keeffe and Hyde (80). As they do not give radii for Fe, Cd, and Co, the data are limited to those structures for which nonbonded radii are available. If the limit of collapse of these structures was the cation–cation contact distance one would expect not to see any points in the top left halves of the plots. While this relationship holds approximately for the smaller tetrahedral frameworks, many of the observed closest M–M distances for the larger frameworks are up to ~ 0.2 Å shorter than predicted, with the greatest discrepancy belonging to Li-containing frameworks, again suggesting that the interstitial cation–oxygen bonding is the limiting factor in framework collapse for stuffed frameworks.

9. TETRAHEDRAL STRING ROTATION AND RESULTANT $\angle M$–O–M ANGLES

The question of the relationship between local $\omega = \angle M$–O–M angles and the tetrahedral string rotation angles θ is a little more complicated than at first glance appears to be the case. Consider the case of rotation around two mutually orthogonal $\langle 110 \rangle_p$ directions—specifically, rotation by θ_x around the $\mathbf{a}_R = [101]_p$ (R = resultant unit cell)

and rotation by θ_z around the $\mathbf{c}_R = [\bar{1}01]_p$ directions (see Fig. 1)—under the assumption of perfectly regular tetrahedra. The resultant $\omega = \angle M$–O–M angles are dependent upon the tetrahedral string rotation angles θ_x and θ_z but cannot be expressed solely as a function of them. The general relationship between the resultant $\omega = \angle M$–O–M angles and the tetrahedral edge rotation angles is in fact a double valued function dependent upon the local rotation pattern.

Consider, for example, $\omega_x = \angle M1$–O1–$M2$ in Fig. 1 (atom labels as for Fig. 1). While the sense of rotation around the O2–O4 tetrahedral edge of the $(M1)O_4$ tetrahedra, i.e., θ_z, automatically determines the sense of rotation of the $(M2)O_4$ tetrahedra around $\mathbf{c}_R$, this is not the case as far as rotation around $\mathbf{a}_R$ or the O1–O3 tetrahedral edge of the $(M1)O_4$ tetrahedra is concerned. There are two distinct possibilities as far as rotation around $\mathbf{a}_R$ is concerned i.e., a "++" rotation pattern or a "+−" rotation pattern (using the notation of Figs. 3 and 6). Note that a "−−" rotation pattern is equivalent to a "++" rotation pattern as far as the local $\angle M$–O–M angle is concerned. Similarly a "−+" rotation pattern is equivalent to a "+−" rotation pattern.

In the former case, the relationship between the resultant $\omega_x = \angle M1$–O1–$M2$ angle and θ_x and θ_z is given by

$$1 - \cos\omega_x = \tfrac{4}{3}(\cos^2\theta_z) + \tfrac{2}{3}(1 + \tan^2\theta_x + \tan^2\theta_z)^{-1}.$$

In the alternative case, the relationship between the resultant $\omega_x = \angle M1$–O1–$M2$ angle and θ_x and θ_z is given by

$$1 - \cos\omega_x = \tfrac{4}{3}(\cos^2\theta_z) + \tfrac{2}{3}(1 + \tan^2\theta_x + \tan^2\theta_z)^{-1} + \tfrac{2}{3}(\sin^2\theta_x \cos^2\theta_x (1 + \tan^2\theta_x + \tan^2\theta_z)).$$

The correction term in the latter expression is quite significant for rotation angles $\sim 20^\circ$ as is typical for cristobalite-related derivative structures, e.g., for $\theta_x = \theta_z = 20^\circ$, $\omega_x = 134.78^\circ$ in the former case and 142.33° in the latter case.

Careful consideration of the different mutually orthogonal rotation patterns known to date (see Figs. 3 and 6) shows that rotation patterns which involve either all "++" or all "+−" configurations such as the β-$KCoO_2$ pattern (B1 in Fig. 3) or the low-cristobalite pattern of (E1 in Fig. 3) might be expected to have only one $\angle M$–O–M angle whereas patterns which involve both "++" as well as "+−" configurations might be expected to have a rather broader spread of $\angle M$–O–M angles.

For certain special cases, this spread can be minimized by making θ_x differ from θ_z. Consider, for example, the β-$NaFeO_2$ rotation pattern (C1 in Fig. 3). Along one unit cell direction there is a "+−+−" rotation pattern whereas along the other unit cell direction the rotation pattern is "++++". Consequently $\angle M$–O–M angles along the former direction should be $\sim 7^\circ$ larger than the $\angle M$–O–M angles along the latter direction when the two tetrahedral edge rotation angles θ_x and θ_z are the same and $\sim 20^\circ$. In practice, this difference in $\angle M$–O–M angles is minimized by making the two rotation angles come apart. A 6° difference in tetrahedral edge rotation angles for example, corresponding to an $\sim 4\%$ split in the resultant cell dimensions, is sufficient for the initial difference in $\angle M$–O–M angles to be eliminated. Such a mechanism for minimizing the spread in resultant $\angle M$–O–M angles cannot work, however, if the rotation pattern contains both "++" as well as "+−" configurations along the same direction e.g., for the $KGaO_2$ rotation pattern (D1 in Fig. 3). In such cases, minimization of the spread in $\angle M$–O–M angles may require distortion of the individual tetrahedra.

10. CUBIC CRISTOBALITE-RELATED STRUCTURES

The problems with a $C9$-type model for β-cristobalite, outlined in Section 1, apply equally to all structures with $Fd\bar{3}m$ (A1) and $F\bar{4}3m$ (A2) symmetry, and as stated in Section 2, it is assumed that these structures are displacively disordered. Presumably this disorder is more static than dynamic at room temperature. Nevertheless, locally, the same concerted rotation of $\langle 110\rangle_p$ tetrahedral strings will be necessary if the framework tetrahedra remain approximately undistorted. For these structures to retain overall cubic symmetry there must be, overall, collapse of the $C9$ parent structure equally along all six $\langle 110\rangle_p$ directions.

The cubic $x = 0.55$ structure in the system $Na_{2-x}Al_{2-x}Si_xO_4$ (81) differs from the above cubic structures in that it is a fully ordered cubic superstructure. Its significance is that, unlike almost all other ordered cristobalite-related derivative structures to date, it can not be derived from the $C9$ type parent structure via concerted rotations of the framework tetrahedra about two mutually orthogonal $\langle 110\rangle_p$ axes, but requires correlated rotations about all six. For this to be possible it is necessary to relax slightly the constraint that the MO_4 tetrahedra remain perfectly regular. It is significant that in the refined model for the $x = 0.55$ structure the deviation from ideality in any one tetrahedron is not great.

The cubic $x = 0.55$ structure teaches us is that it is possible to generate fully ordered collapsed $C9$ structural models that include concerted rotation about more than two $\langle 110\rangle_p$ tetrahedral edges simultaneously. Although there are no known examples to date, the possibility of rhombohedral, trigonal or other derivative structures arising from simultaneous concerted rotations about more than two $\langle 110\rangle_p$ tetrahedral edges can not be ruled out. However, on the basis of observations to date, structures involving rotations about more than two edges appear to be rare.

11. DISORDER, STACKING FAULTS, AND DISPLACIVE PHASE TRANSITIONS

Given the available evidence, it seems reasonable to presume that the high temperature phases of all cristobalite-related derivative structures are characterized by dynamically disordered $\langle 110 \rangle_p$ tetrahedral edge rotation patterns. The experimental electron diffraction result that all modulation wave-vectors normal to a particular $\langle 110 \rangle_p$ tetrahedral edge direction are equally excited in these high temperature phases implies that all possible tetrahedral edge rotation patterns (including many not shown in Fig. 3, i.e., which do not occur as long-range ordered, low temperature, derivative structures) must occur at least instantaneously in these high temperature phases.

On cooling down from high temperature, it would therefore be surprising if remnants of this high temperature dynamical disorder did not remain in the low temperature derivative structures in the form of microstructural defects. Unfortunately the sensitivity of most cristobalite-related phases to electron beam irradiation makes imaging studies of such microstructural defects rather difficult. Direct imaging evidence for the existence of such microstructure is only available in the case of low cristobalite as far as the current authors are aware. Possible such defects in the case of low cristobalite include pseudomerohedral twin boundaries between tetragonal twin variants, displacements faults within variants, and enantiomorphic twinning within variants (7, 82, 83).

Pseudomerohedral twin boundaries are usually relatively easily detected as a result of the strain distortion accompanying the particular tetrahedral edge rotation pattern responsible for the lowering in point group symmetry from *m*3*m*. Rather more subtle and interesting from the rotation pattern point of view are defects which involve flipping the sign of tetrahedral edge rotation patterns about one or other of the two mutually orthogonal $\langle 110 \rangle$ tetrahedral edges about which rotation is taking place. In the case of low cristobalite, for example, such a boundary corresponds to a $P4_12_12$ to $P4_32_12$ enantiomorphic twin boundary (see, for example, Fig. 14). The ubiquitous presence of these twin boundaries in the case of low cristobalite suggests that they may well be endemic in many cristobalite-related derivative structures, in particular, those that are grown from high temperature. By contrast cristobalite-related derivative structures that are grown at low temperatures (hydrothermally grown *m*-Na_2MgSiO_4, for example (19) may well be less defective.

Such faulting is important because it is likely that the regions on either side of such a fault will scatter coherently so that the effective rotation amplitude found by either single crystal or powder structure refinement will be correspondingly reduced. Indirect evidence for the existence of such faulting has been found in various cristobalite-related derivative structures (16, 17, 81). In the case of low cristobalite, one would expect and finds that such faulting can occur across any curved surface that includes either the $[100]_{tet.}$ or the $[010]_{tet.}$ (tet. = tetragonal α-cristobalite unit cell) directions. From E in Fig. 3 it is clear that such a fault locally generates a two-layer slab of the β-$NaFeO_2$ structure type (cf. C and E in Fig. 3).

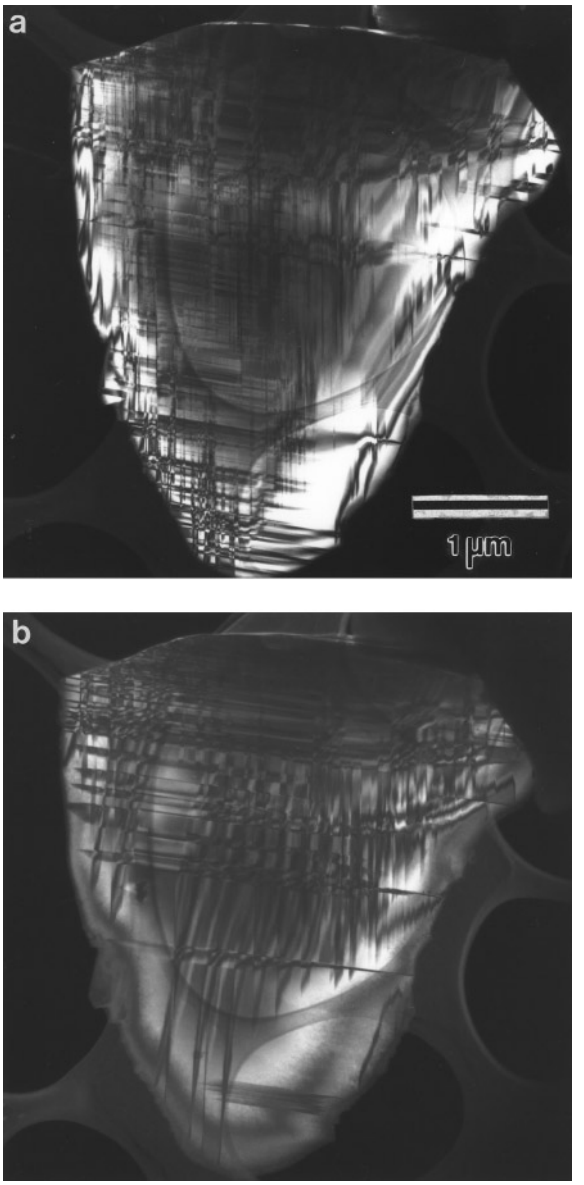

FIG. 14. Low-magnification TEM satellite dark-field image of α-cristobalite taken in the close vicinity of the $[112]_{tet.}$ zone axis and utilising operating reflection $\mathbf{g} = [1\bar{1}0]^*_{tet.}$, (a) before and (b) after cycling through the $\alpha \leftrightarrow \beta$ phase transition. Note that the enantiomorphic twin boundaries show no memory effect on cycling through the phase transition.

12. CONCLUSIONS

By describing cristobalite-related structures in terms of concerted rotations of $\langle 110 \rangle_p$ tetrahedral strings about two mutually orthogonal $\langle 110 \rangle_p$ axes we now have a unified picture of this diverse family of compounds with structures derived from the *C*9 structure type. Not only is the mechanism of distortion simple but it is the very mechanism which underpins the dynamically disordered model of β-cristobalite, the type compound.

Using this description it has been possible to classify all known cristobalite-related oxide structures, with only one recently discovered exception, in terms of their patterns of rotation and to predict other relatively simple structures which have not yet been observed. Interestingly, the six simplest patterns of rotations are now represented by known refined structures.

We have deliberately avoided classification according to space group symmetry because of a lack of uniqueness of structure by this approach (see Table 1) and inevitable confusion created by choice of setting and origin. Identifying structures in terms of patterns of $+$'s and $-$'s avoids both of these problems.

The main insights into the crystal chemistry of cristobalite-related oxides to be gleaned from this review are summarised below:

(i) While it is useful to consider MO_4 tetrahedra as perfectly regular, rigid units when modeling the concerted collapse of the *C*9 structure, there is substantial evidence that the MO_4 tetrahedra in cristobalite-related oxides readily accommodate significant distortion. The only types of cristobalite-related structures that behave as if they comprise regular, rigid units are the fully Na stuffed α-cristobalite-type and β-$NaFeO_2$-type (see Figs. 10 and 11). This apparently ideal behavior is, however, equally attributable to the full occupancy of the interstitial sites by the ideally sized Na cations as it is to strong intratetrahedra bonding and nonbonding interactions constraining MO_4 tetrahedra to be regular. The nonideal behavior, in general, of the partly stuffed and unstuffed structures supports this view. Nevertheless, as a first approximation all cristobalite-related oxides can be considered as consisting of regular, rigid MO_4 tetrahedra.

(ii) In the fully or partly stuffed structures it is the size or bonding requirements of the interstitial cations which determines the degree of collapse of the *C*9 framework. Cation–cation contacts, defined as the sum of the two nonbonded atomic radii, *R*, of O'Keeffe and Hyde (80), do not appear to be a limiting factor. It is not clear from correlations presented in this study what the limiting factor is in the collapse of the unstuffed structures.

(iii) For cristobalite-related oxides showing approximately ideal collapse behavior where symmetry allows for more than one $\angle M$–O–M angle, the two rotation angles θ_x and θ_z diverge so as to make the two $\angle M$–O–M angles equal. The only example of a group of compounds that displays such behavior is the fully Na stuffed β-$NaFeO_2$-type structures (see Fig. 10). While some other refined structures whose symmetry generates more than one $\angle M$–O–M angle display a tendency to make $\angle M$–O–M angles equal, their nonideal MO_4 tetrahedra make a relationship between $\angle M$–O–M angle and rotation angles θ_x and θ_z less meaningful. However, given regular, rigid tetrahedra it is impossible for structure types with rotation patterns containing "$++--$" and "$+++-$" motifs to adjust the two rotation angles θ_x and θ_z to make all $\angle M$–O–M angles equal.

(iv) Because all patterns of concerted rotations of $\langle 110 \rangle_p$ tetrahedral strings are necessarily to a first approximation equal in energy, stacking faults and displacive disorder are likely to be endemic in such structures. For those materials synthesized in the stability field of the final distorted structure, e.g., via hydrothermal synthesis at relatively low temperatures, crystal perfection is much more likely. However, as most reported cristobalite-related oxides are synthesised at high temperature, presumably above a displacive phase transition in most cases, one would expect significant faulting and/or disorder.

The one exception to this unifying description of concerted rotations of the framework tetrahedra about two mutually orthogonal $\langle 110 \rangle_p$ axes is the cubic $x = 0.55$ structure in the system $Na_{2-x}Al_{2-x}Si_xO_4$ (81). This structure requires correlated rotations about all six $\langle 110 \rangle_p$ axes and is only able to be modelled by relaxing slightly the constraint that the MO_4 tetrahedra remain perfectly regular. By releasing this constraint other as yet unreported structure types are conceivable involving concerted rotations about more than two $\langle 110 \rangle_p$ axes simultaneously.

It is inevitable that there will be future discoveries of new cristobalite-related phases with both old and new structure types. This is a consequence of the inherent displacive flexibility of the *C*9 framework and its subsequent ability to accommodate a wide range of chemical compositions. What can be predicted with reasonable certainty is that the structural principles of the known structure types which have been described in this review will also apply to any new structure types.

REFERENCES

1. R. W. G. Wyckoff, *Am. J. Sci.* **9,** 448 (1925).
2. R. W. G. Wyckoff, *Z. Kristallogr.* **62,** 189 (1925).
3. M. O'Keeffe and B. G. Hyde, *Acta Crystallogr., Sect. B* **32,** 2923 (1976).
4. A. F. Wright and A. J. Leadbetter, *Philos. Mag.* **31,** 1391 (1975).
5. D. M. Hatch and S. Ghose, *Phys. Chem. Miner.* **17,** 554 (1991).
6. G.-L. Hua, T. R. Welberry, R. L. Withers, and J. G. Thompson, *J. Appl. Crystallogr.* **21,** 458 (1988).
7. R. L. Withers, J. G. Thompson, and T. R. Welberry, *Phys. Chem. Mineral.* **16,** 517 (1989).

8. T. R. Welberry, G.-L. Hua, and R. L. Withers, *J. Appl. Crystallogr.* **22,** 87 (1989).
9. M. T. Dove, V. Heine, and K. D. Hammonds, *Mineral. Mag.* **59,** 629 (1995).
10. K. D. Hammonds, M. T. Dove, A. P. Giddy, V. Heine, and B. Winkler, *Am. Mineral.* **81,** 1057 (1996).
11. B. L. Phillips, J. G. Thompson, Y. Xaio, and R. J. Kirkpatrick, *Phys. Chem. Miner.* **20,** 341 (1993).
12. K. S. Finnie, J. G. Thompson, and R. L. Withers, *J. Phys. Chem. Solids* **55,** 23 (1994).
13. I. P. Swainson and M. T. Dove, *Phys. Rev. Lett.* **71,** 193 (1993).
14. I. P. Swainson and M. T. Dove, *J. Phys.: Condens. Matter* **7,** 1771 (1995).
15. R. L. Withers and J. G. Thompson, *Acta Crystallogr., Sect. B* **49,** 614 (1993).
16. R. L. Withers, C. Lobo, J. G. Thompson, S. Schmid, and R. Stranger, *Acta Crystallogr., Sect. B* **53,** 203 (1997).
17. J. G. Thompson, R. L. Withers, A. Melnitchenko, and S. R. Palethorpe, *Acta Crystallogr., Sect. B* (in press).
18. J. A. Kaduk and S. Pei, *J. Solid State Chem.* **115,** 126 (1995).
19. W. H. Baur, T. Ohta, and R. D. Shannon, *Acta Crystallogr., Sect. B* **37,** 1483 (1981).
20. C. Delmas, C. Foussier, and P. Hagenmuller, *J. Solid State Chem.* **13,** 165 (1975).
21. M. Marezio and J. P. Remeika, *J. Chem. Phys.* **44,** 3348 (1966).
22. D. R. Peacor, *Z. Kristallogr.* **138,** 274 (1973).
23. Z. Tomkowicz and A. Szytuka, *J. Phys. Chem. Solids* **38,** 1117 (1977).
24. C. Li, A. F. Reid, and S. Saunders, *J. Solid State Chem.* **3,** 614 (1971).
25. L. T. Brownmiller, *Am. J. Sci.* **29,** 260 (1935),
26. K. Kosten and H.Arnold, *Z. Kristallogr.* **152,** 119 (1980).
27. J. V. Smith and O. V. Tuttle, *Am. J. Sci.* **255,** 282 (1957).
28. E. W. Roedder, *Am. J. Sci.* **249,** 224 (1951).
29. T. F. W. Barth and E. Posnjak, *Z. Kristallogr.* **81,** 370 (1932).
30. L. M. Torres-Martinez and A. R. West, *J. Mater. Sci. Lett.* **7,** 821 (1988).
31. C. Colbeau-Justin, G. Wallez, A. Elfakir, M. Quarton, and E. Suard, *J. Solid State Chem.* **134,** 59 (1997).
32. A. Grund, *Tschermaks Mineral. Petrogr. Mitt.* **5,** 227 (1955).
33. G. E. R. Schulze, *Z. Phys. Chem., Abt. B* **24,** 215 (1934).
34. R. C. L. Mooney, H. Kissinger, and A. Perloff, *Acta Crystallogr.* **7,** 642 (1954).
35. J. Liebertz and S Stähr, *Z. Kristallogr.* **155,** 115 (1981).
36. F. Bertaut and P. Blum, *C. R. Acad. Sci. Paris* **239,** 429 (1954).
37. I. E. Grey, B. F. Hoskins, and I. C. Masden, *J. Solid State Chem.* **85,** 202 (1990).
38. E. von Vielhaber and R. Hoppe, *Z. Anorg. Allg. Chem.* **369,** 14 (1969).
39. C. Delmas, A. Maazaz, and P. Hagenmuller, *Solid State Ionics* **9–10,** 83 (1983).
40. M. Marezio, *Acta Crystallogr.* **18,** 481 (1965).
41. C. A. Joubert-Bettan, R. Lachenal, E. F. Bertaut, and E. Parthé, *J. Solid State Chem.* **1,** 1 (1969).
42. G. F. Plakhov and N. V. Belov, *Sov. Phys. Crystallogr.* **24**(6), 674 (1979).
43. J. Grins, *Chem. Scr.* **28,** 111 (1988).
44. J. Grins and M. Nygren, *Solid State Ionics* **9–10,** 869 (1983).
45. É. A. Kuz'min, V. V. Ilyukhin, and N. V. Belov, *Sov. Phys. Crystallogr.* **13**(6), 848 (1969).
46. G. Vaivars, J. Grins, and T. Hörlin, *Solid State Ionics* **78,** 259 (1995).
47. J. Grins, T. Hörlin, and G. Vaivars, *Solid State Ionics* **89,** 1 (1996).
48. A. Maazaz and C. Delmas, *Solid State Ionics* **6,** 261 (1982).
49. J. G. Thompson, A. Melnitchenko, S. R. Palethorpe, and R. L. Withers, *J. Solid State Chem.* **131,** 24 (1997).
50. C. M. Foris, F. C. Zumsteg, and R. D. Shannon, *J. Appl. Crystallogr.* **12,** 405 (1979).
51. S. Hipert and A. Linder, *Z. Phys. Chem.* **22,** 395 (1933).
52. C. W. F. T. Pistorius and G. F. de Vries, *Z. Anorg. Allg. Chem.* **395,** 119 (1973).
53. S. Frostäng, J. Grins, and M. Nygren, *Chem. Scr.* **28,** 107 (1988).
54. J. Grins, *Solid State Ionics* **7,** 157 (1982).
55. JCPDS File No. 49-8.
56. S. Frostäng, J. Grins, and M. Nygren, *Solid State Ionics* **44,** 51 (1990).
57. J. Grins, *Solid State Ionics* **18–19,** 577 (1986).
58. S. Frostäng, J. Grins, and M. Nygren, *Solid State Ionics* **28–30,** 237 (1988).
59. B. Maksimov, R. Tamazyan, M. I. Sirota, S. Frostäng, J. Grins, and M. Nygren, *J. Solid State Chem.* **86,** 64 (1990).
60. S. Frostäng and P.-E. Werner, *Mater. Res. Bull.* **24,** 833 (1989).
61. S. Frostäng, J. Grins, D. Louër, and P.-E. Werner, *Solid State Ionics* **31,** 131 (1988).
62. J. Grins and D. Louër, *J. Solid State Chem.* **87,** 114 (1990).
63. J. Grins, *Mater. Res. Bull.* **25,** 371 (1990).
64. C. Colbeau-Justin, G. Wallez, A. Elfakir, and M. Quarton, *Powder Diffract.* **12,** 138 (1997).
65. W. A. Dollase, *Z. Kristallogr.* **121,** 369 (1965).
66. J. Théry and D. Briancon, *Rev. Hautes Temp. Refract.* **1,** 221 (1964).
67. I. E. Grey and C. Li, *J. Solid State Chem.* **69,** 116 (1987).
68. M. Marezio, *Acta Crystallogr.* **19,** 396 (1965).
69. E. F. Bertaut, A. Delapalme, G. Bassi, A. Darif-Varabon, and J. C. Joubert, *Bull. Soc. Fr. Mineral. Crist.* **88,** 103 (1965).
70. K. J. Seifert, H. Nowotny, and E. Hauser, *Mh. Chem.* **102,** 1006 (1971).
71. R. A. Howie and A. R. West, *Acta Crystallogr., Sect. B* **30,** 2434 (1974).
72. H. N. Ng and C. Calvo, *Can. J. Phys.* **55,** 677 (1977).
73. R. C. L. Mooney, *Acta Crystallogr.* **9,** 728 (1956).
74. Y. A. Kharitonov, V. M. Golyshev, R. K. Rastsvetaeva, and N. V. Belov, *Sov. Phys. Crystallogr.* **19,** 667 (1974).
75. J. Grins, L. Eriksson, and Y. Kanno, *Solid State Ionics* **92,** 293 (1996).
76. E. Parthé, K. Yvon, and R. H. Deitch, *Acta Crystallogr., Sect. B* **25,** 1164 (1969).
77. A. R. West, *Z. Kristallogr.* **141,** 422 (1975).
78. I. D. Brown and D. Altermatt, *Acta Crystallogr., Sect. B* **41,** 244 (1985).
79. N. E. Brese and M. O'Keeffe, *Acta Crystallogr., Sect. B* **47,** 192 (1991).
80. M. O'Keeffe and B. G. Hyde, *Struct. Bonding Crystals* **1,** 227 (1981).
81. R. L. Withers, J. G. Thompson, A. Melnitchenko, and S. R. Palethorpe, *Acta Crystallogr., Sect. B* (in press).
82. J. M. Christie, J. S. Lally, A. H. Heuer, R. M. Fisher, D. T. Griggs, S. V. Griggs, and S. V. Radcliffe, *Proc. Lunar Sci. Conf., 2nd*, **1,** 69–89 (1971).
83. R. L. Withers and J. G. Thompson, *in* "In Situ and Recent Advances in Electron Microscopy," Chap. 13, pp. 301–330. Kluwer, Boston, 1997.